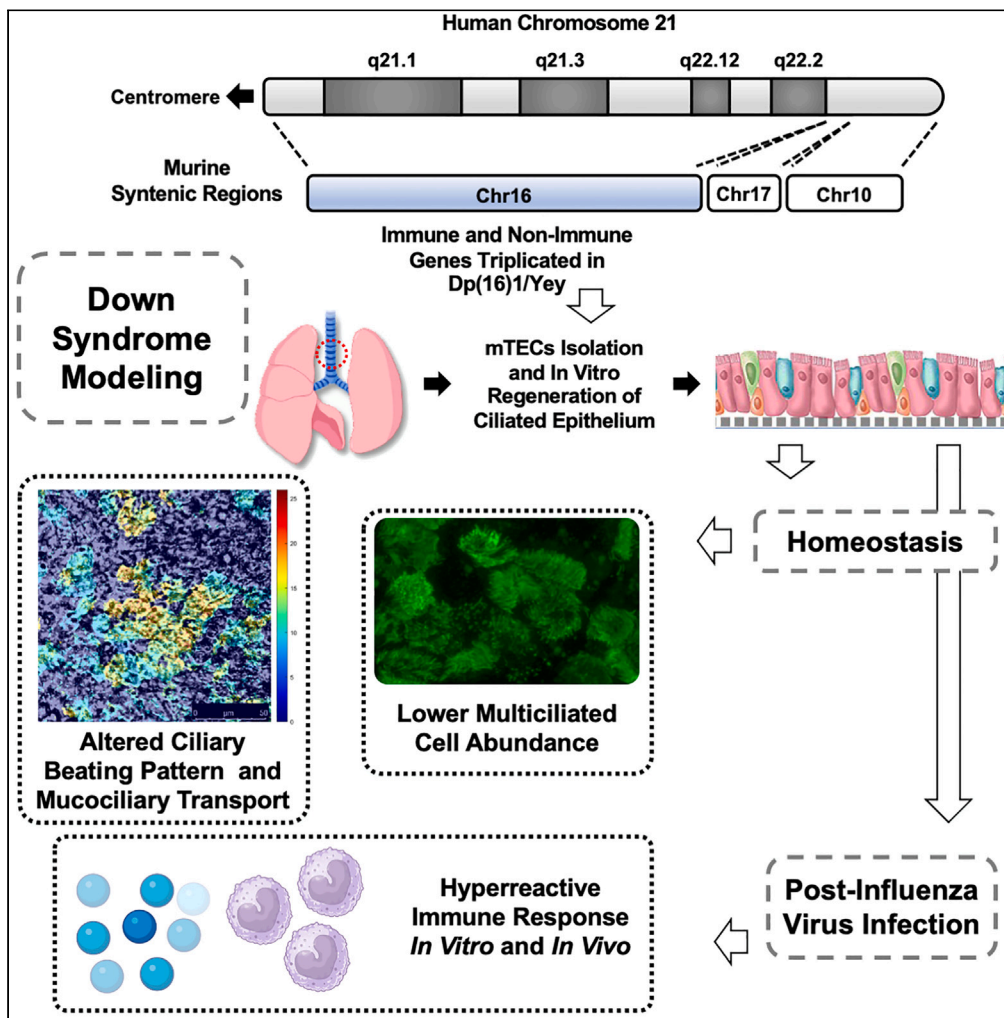


Article

Down syndrome is associated with altered frequency and functioning of tracheal multiciliated cells, and response to influenza virus infection



Samantha N. Thomas, Brian F. Niemeyer, Rocio J. Jimenez-Valdes, ..., Rodrigo Cañas-Arranz, Adolfo García-Sastre, Kambez H. Benam

benamk@pitt.edu

Highlights

Dp16 vs. WT mTECs have lower ciliated cells, altered CBF, and reduced MCT

Dp16 vs. WT mTECs show an immune hyperreactive phenotype post-IAV challenge *in vitro*

Dp16 mice show immune hyperresponsiveness following infection with IAV *in vivo*



## Article

## Down syndrome is associated with altered frequency and functioning of tracheal multiciliated cells, and response to influenza virus infection

Samantha N. Thomas,<sup>1,14</sup> Brian F. Niemeyer,<sup>2,14</sup> Rocío J. Jimenez-Valdes,<sup>2</sup> Alexander J. Kaiser,<sup>1</sup> Joaquin M. Espinosa,<sup>3,4</sup> Kelly D. Sullivan,<sup>3,5</sup> Andrew Goodspeed,<sup>4,6</sup> James C. Costello,<sup>3,4,6</sup> Jonathan K. Alder,<sup>2</sup> Rodrigo Cañas-Arranz,<sup>7</sup> Adolfo García-Sastre,<sup>7,8,9,10,11</sup> and Kambez H. Benam<sup>2,3,12,13,15,\*</sup>

## SUMMARY

**Individuals with Down syndrome (DS) clinically manifest severe respiratory illnesses; however, there is a paucity of data on how DS influences homeostatic physiology of lung airway, and its reactive responses to pulmonary pathogens. We generated well-differentiated ciliated airway epithelia using tracheas from wild-type and Dp(16)1/Yey mice *in vitro*, and discovered that Dp(16)1/Yey epithelia have significantly lower abundance of ciliated cells, an altered ciliary beating profile, and reduced mucociliary transport. Interestingly, both sets of differentiated epithelia released similar quantities of viral particles after infection with influenza A virus (IAV). However, RNA-sequencing and proteomic analyses revealed an immune hyperreactive phenotype particularly for monocyte-recruiting chemokines in Dp(16)1/Yey epithelia. Importantly, when we challenged mice *in vivo* with IAV, we observed immune hyper-responsiveness in Dp(16)1/Yey mice, evidenced by higher quantities of lung airway infiltrated monocytes, and elevated levels of pro-inflammatory cytokines in bronchoalveolar lavage fluid. Our findings illuminate mechanisms underlying DS-mediated pathophysiological changes in airway epithelium.**

## INTRODUCTION

Trisomy 21 (T21), the cause of DS, is the most prevalent human chromosomal disorder. Pneumonia and infectious lung disease are a leading cause of death in T21. Respiratory disease is second only to congenital heart defect in mortality of children with T21<sup>1</sup>; children with DS exhibit increased susceptibility to lower respiratory tract infections,<sup>2</sup> and have significantly elevated risk of mortality from sepsis (after adjusting for potential confounding factors).<sup>3</sup> In fact, lower respiratory tract pathology has been reported as the most common cause of acute hospital admission,<sup>4</sup> and it has been reported that persons with DS have 4- and 10-fold increased risk for coronavirus disease 2019 (COVID-19)-related hospitalization and death, respectively.<sup>5</sup> Moreover, it has been shown that children with DS exhibit significantly higher chances of having airway physical anomalies (such as laryngomalacia, tracheomalacia and combined malformation) compared with control subjects on endoscopic examination,<sup>6</sup> which in turn may contribute to increase sensitivity to respiratory infection.

It is well-documented that people with DS display lifelong immune dysregulation. There are multiple genes encoded on human chromosome 21 (chr21) with roles in immune control, including four of the six interferon receptor (IFNR) genes.<sup>7</sup> It has been shown that IFN signaling is consistently activated by T21 in multiple human cell types,<sup>7</sup> and levels of many pro-inflammatory cytokines such as IL6, MCP1, and TNF $\alpha$  are elevated in peripheral blood of individuals with DS.<sup>8</sup> Similarly, mass cytometry approaches have uncovered global immune dysregulation in people with T21, with changes in lymphoid and myeloid compartments as well as upregulation of surface protein expression of a key IFNR (IFNAR1) on circulating leukocytes.<sup>9</sup> Altogether, these findings support the notion of immune dysregulation and hyperactivity as potential drivers of the differential disease spectrum in DS.

However, there is a paucity of data on how exactly T21 influences homeostatic physiology of lung airway, which is the primary target of many inhaled respiratory pathogens, and its reactive responses to infection

<sup>1</sup>Department of Bioengineering, University of Colorado Denver, Aurora, CO 80045, USA

<sup>2</sup>Division of Pulmonary, Allergy, and Critical Care Medicine, Department of Medicine, University of Pittsburgh, Pittsburgh, PA 15213, USA

<sup>3</sup>Linda Crnic Institute for Down Syndrome, University of Colorado, Anschutz Medical Campus, Aurora, CO 80045, USA

<sup>4</sup>Department of Pharmacology, University of Colorado Anschutz Medical Campus, Aurora, CO 80045, USA

<sup>5</sup>Department of Pediatrics, University of Colorado Anschutz Medical Campus, Aurora, CO 80045, USA

<sup>6</sup>University of Colorado Comprehensive Cancer Center, University of Colorado Anschutz Medical Campus, Aurora, CO 80045, USA

<sup>7</sup>Department of Microbiology, Icahn School of Medicine at Mount Sinai, New York, NY 10029, USA

<sup>8</sup>Department of Medicine, Division of Infectious Diseases, Icahn School of Medicine at Mount Sinai, New York, NY 10029, USA

<sup>9</sup>Global Health and Emerging Pathogens Institute, Icahn School of Medicine at Mount Sinai, New York, NY 10029, USA

<sup>10</sup>The Tisch Cancer Institute, Icahn School of Medicine at Mount Sinai, New York, NY 10029, USA

<sup>11</sup>Department of Pathology, Molecular and Cell-Based Medicine, Icahn School of Medicine at Mount Sinai, New York, NY 10029, USA

Continued



with pulmonary pathogens. As such, here we focused on two specific aims: (1) whether distribution of airway epithelial cell subtypes and epithelial cell function is altered in DS and (2) if airway epithelial cells in DS respond differently compared with disomic controls when infected with influenza A virus (IAV) – a representative respiratory infectious agent. To address these aims, we utilized murine tracheal epithelial cells (mTECs) isolated from wild-type (WT) and Dp(16)1/Yey<sup>10</sup> (hereafter referred to as Dp16) mice, an advanced mouse model of T21 carrying triplication of ~120 genes syntenic to human chr21. For studies in aim (1), we examined abundance of multiciliated cells, as a major epithelial subtype (by microscopic immunofluorescent staining and flow cytometry) in the mTECs differentiated *in vitro* under air-liquid interface (ALI). We also evaluated barrier function (by trans-epithelial electrical resistance [TEER] measurement), ciliary beating frequency (CBF) pattern (by high-frequency imaging) and mucociliary transport (MCT) (by analysis of fluorescent nanoparticle displacement) of the Dp16 vs. WT epithelia. For studies in aim (2), we studied virus shedding from luminal surface of mTECs infected with IAV (by real-time qPCR) and characterized inflammatory immune response (by bulk RNA-seq and secreted cytokine/chemokine analysis). In addition, we performed *in vivo* studies to confirm the *in vitro* findings.

## RESULTS

### Validity of Dp16 murine model *in vitro*, epithelial cell differentiation, cellular subtypes distribution, and barrier function

Currently, it is extremely challenging to obtain lung tissue from individuals with DS. Thus, for our studies we employed a mouse model of DS known as Dp16 and its WT littermates for isolation of mTECs. The regions on human chr21 are syntenically conserved with three regions located on mouse chromosomes 10, 16, and 17 (Figure 1A); and Dp16 mice carry triplication of ~2/3 of murine homologs of human chr21 genes,<sup>10</sup> including the four IFNRs, hence their selection for this study. The mTECs from WT and Dp16 mice were cultured at passage 0 (P0) on tissue culture transwell inserts and guided to full differentiation into ciliated epithelial under ALI to evaluate homeostatic differences between the two conditions (Figure 1B). To ensure our cultures were not contaminated with hematopoietic cells, we immunostained the cells (by flow cytometry) following isolation from tracheas and prior to seeding into the transwell culture inserts and found that isolated cells are >99.9% non-hematopoietic (Figure 1C); gating strategy is shown in Figure S1A. We then cultured the mTECs *in vitro* and by day 21 post-ALI, we observed terminal epithelial differentiation; thus, to validate maintenance of murine chr16 (Mmu16) triplication in our model system, we lysed the cells at this point and sequenced the RNA (bulk RNA-seq). We observed increased expression levels (~1.5-fold) of select immune genes on Mmu16 (e.g., *Ifnar1*, *Ifnar2*, *Ifngr2*, *Il10rb* and *Tmprss2*) in Dp16 mTECs compared with WT controls (Figure 1D). These five genes are located on murine chr16. The significantly increased expression of these genes represents two important points: (1) the Dp16 mice used in our studies retained Mmu16 triplication and this was not impacted by isolation process and *in vitro* culture and differentiation of the mTECs and (2) the human orthologs of these genes are located on chr21 and as such their enhanced expression mimics what is seen in people with DS (can be affected by the extent of chromosomal triplication). Notably, we did not expect these genes to show an FC > 2 in Dp16 vs. WT; rather we anticipated approximately 1.5-fold (significant) increase in their expression in Dp16 mTECs as the mice from which the epithelial cells were isolated should have three (instead of two) copies of each gene. In addition, the cells from both groups of mice formed a tight barrier (evident by high TEER) and maintained it throughout the culture (Figure 1E). On days 8 and 22 there were modestly higher values of TEER in WT epithelia compared with Dp16 that reached statistical significance; but overall, the TEER pattern was very similar between the two conditions and remained >1,000 Ω cm<sup>2</sup> post-ALI, indicating that T21 is unlikely to negatively impact the ability of mTECs to form a tight barrier during regeneration.

We then asked whether abundance of multiciliated epithelial cells is altered in this murine *in vitro* model of T21. As shown in Figure 1F, quantitative analysis by flow cytometry revealed that the number of β-tubulin IV-positive keratin 5-negative ciliated cells was significantly lower in Dp16 epithelia compared with WT (gating strategy is shown in Figure S1B). We then confirmed this observation by confocal microscopic imaging of immunostained cultures and found a similar trend (Figure 1G). In addition, we performed immunostaining and confocal microscopic imaging (Figure S2) to gain insight into the number of cilia per multiciliated cells and its change in Dp16 vs. WT mTECs in an indirect and semi-quantitative manner. We picked this approach (as opposed to electron microscopy) due to its higher feasibility and higher throughput for analysis (enabling study of many multiciliated cells).

<sup>12</sup>Department of Bioengineering, University of Pittsburgh, Pittsburgh, PA 15219, USA

<sup>13</sup>Vascular Medicine Institute, University of Pittsburgh, Pittsburgh, PA 15213, USA

<sup>14</sup>These authors contributed equally

<sup>15</sup>Lead contact

\*Correspondence: [benamk@pitt.edu](mailto:benamk@pitt.edu)

<https://doi.org/10.1016/j.isci.2023.107361>

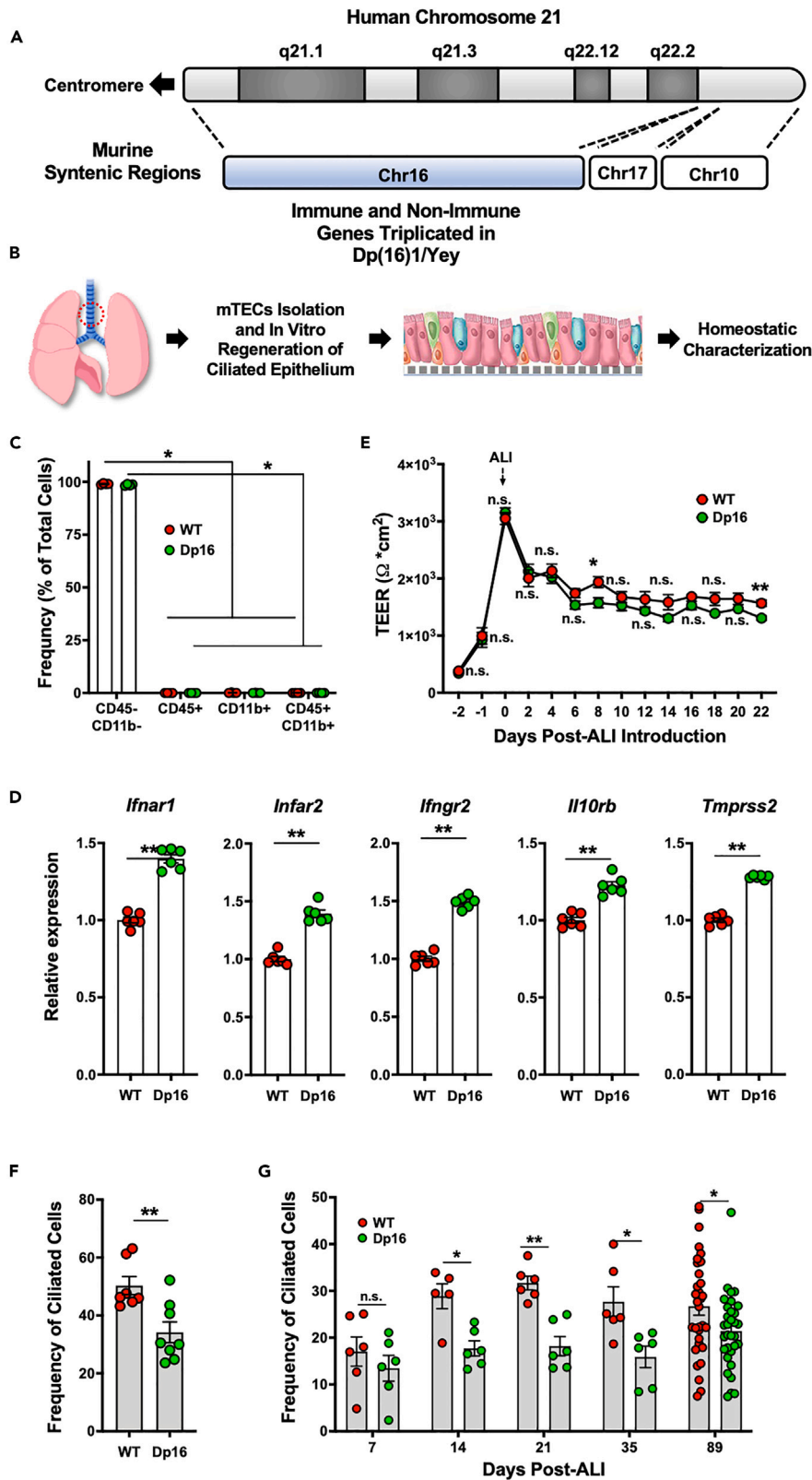


**Figure 1. Altered Multiciliated Cell Abundance in Lung Airway Epithelium of Murine Down Syndrome Model**

(A) Diagram illustrating long arm of human chromosome 21 (chr21) and its orthologous regions on chromosomes 16, 17 and 10 in mice. Note the majority of the genes are located on chr16 in mice which is triplicated in Dp(16)1/Yey (Dp16) mouse model.

(B) Schematic of our experimental approach. In brief, we isolated murine tracheal epithelial cells (mTECs) from lungs of wild-type (WT) and Dp16 mice and cultured at P0 *in vitro* atop porous membranes and guided to terminal differentiation into ciliated epithelia under air-liquid interface (ALI). At day 21 (D21) post-ALI the mature ciliated epithelia were compared for homeostatic differences.

(C) Flow cytometry analysis showed that almost all cells (>99%) following isolation from tracheas and prior to seeding into transwell insert medium with epithelial culture medium are of non-hematopoietic origin (n = 4 × tracheas per group [WT and Dp16]; analyzed by non-parametric *Mann-Whitney* test).

(D) Relative expression of select genes which are located on murine syntenic region on chromosome 16 and triplicated in Dp16 model were plotted based on RNA-seq data. *Ifnar1*: Interferon Alpha and Beta Receptor Subunit 1 gene; *Ifnar2*: Interferon Alpha and Beta Receptor Subunit 2 gene; *Ifngr2*: Interferon Gamma Receptor 2 gene; *Il10rb*: Interleukin 10 Receptor Subunit Beta gene; *Tmprss2*: Transmembrane Serine Protease 2 gene (n = 6 × mTEC transwell inserts [TWIs] per group [WT and Dp16]; analyzed by non-parametric *Mann-Whitney* test).

(E) WT and Dp16 mTECs exhibited overall very similar *trans*-epithelial electrical resistance (TEER) during *in vitro* culture and differentiation. TEER measurements ( $\Omega \cdot \text{cm}^2$ ) were collected daily from two days prior to ALI and then ever two days until D22 post-ALI. Note the tight barrier function induction on day of ALI induction and its maintenance throughout culture for both epithelia. Only on D8 and D22 post-ALI, TEER was modestly and significantly higher in WT compared with Dp16 (n = 12 × transwell inserts per group [WT and Dp16]; two independent experiments; analyzed by non-parametric *Mann-Whitney* test).

(F) Flow cytometry analysis on abundance of ciliated cells (defined as  $\beta$ -tubulin IV<sup>+</sup> Keratin 5<sup>-</sup>) in well-differentiated non-infected and infected WT vs. Dp16 epithelia on D21 post-ALI (n = 7–8 × TWIs per group [WT and Dp16]; two independent experiments; analyzed by non-parametric *Mann-Whitney* test). Note lower frequency of the ciliated cells in well-differentiated Dp16 mTECs.

(G) Time course characterization of  $\beta$ -tubulin IV<sup>+</sup> cells on days 7, 14, 21 and 89 post-ALI (studied by confocal image analysis of immunostained samples) showed that the number of ciliated cells was significantly lower at all time points in Dp16 vs. WT epithelia (n = 5–10 × WT TWIs and n = 6–10 × Dp16 TWIs each with 1–8 fields of view (datapoint) imaged; analyzed by non-parametric *Mann-Whitney* test). \*p < 0.05, \*\*p < 0.01, n.s., not significant. Data represent mean and s.e.m. See also [Figures S1](#) and [S2](#).

**Ciliary function**

Interrogating ciliary function, we next investigated the impact of T21 on epithelial CBF pattern and MCT ([Figure 2](#); [Table 1](#)). To capture a detailed, high-resolution view of the CBF, we acquired videos of ciliary beating using a high-speed camera while the cells were maintained in a humidified 37°C, gas-balanced tissue culture chamber, and analyzed the recordings with a custom-written Matrix Laboratory (MATLAB) code. The code analyzes each video frame-by-frame, pixel-by-pixel and detects active areas of movement within the video as well as the oscillating frequency of the movements observed. These data are then used to generate a heatmap for each video, which displays binned distribution of CBF with color codes each representing a distinct beating rate (in Hz) ([Figure 2A](#)). The major advantage of our analytical strategy compared with manual or semi-automated quantification of CBF based on slowed-down video recordings is that we apply user-unbiased machine-applied acquisition of every single cilium beating – that is per cilium, per cell, per field of view, per replicate, per condition. In our studies we discovered differential patterns of CBF in WT vs. Dp16 mTECs. For instance, we observed that WT compared with Dp16 epithelia exhibit a larger range of ciliary beating (24 [3–27 Hz] vs. 22 [3–25 Hz]) and higher CBF median (12 Hz vs. 10 Hz) ([Figure 2B](#); [Table 1](#)). We chose to compare the median between the two epithelial types as all the acquired CBF recordings (including the infected mTECs), despite a Gaussian-like distribution ([Figure 2B](#)), failed normality when analyzed by multiple tests ([Table 1](#); [Figure S3](#)). Interestingly, skewness (a measure of a dataset’s symmetry) and kurtosis (which quantifies whether the tails of the data distribution match the Gaussian distribution) were also different between the WT and Dp16 mTECs ([Figure 2C](#); [Table 1](#)). WT epithelia had CBF skewness of 0.3378 (unitless) compared with 0.4552 in Dp16 counterparts. A symmetrical distribution has a skewness of 0, and an asymmetrical distribution with a long tail to the right (i.e., higher CBF values) has a positive skew. Thus, both epithelia have asymmetrical ciliary beating distribution – consistent with lack of normality; however, the Dp16 mTECs show slightly increased skewness to higher CBF values, meaning the right tail of the distribution is longer than the left and such more of the ciliary beatings occur at lower rates – consistent with lower median CBF in the epithelial cells. Kurtosis (unitless) is a measure of deviation from a normal distribution at extreme values. A Gaussian distribution has a kurtosis of 0; a distribution with fewer values in the tails than a Gaussian distribution has a negative kurtosis, and a distribution with more values in the tails than a Gaussian distribution has a positive kurtosis. The CBF profiles in

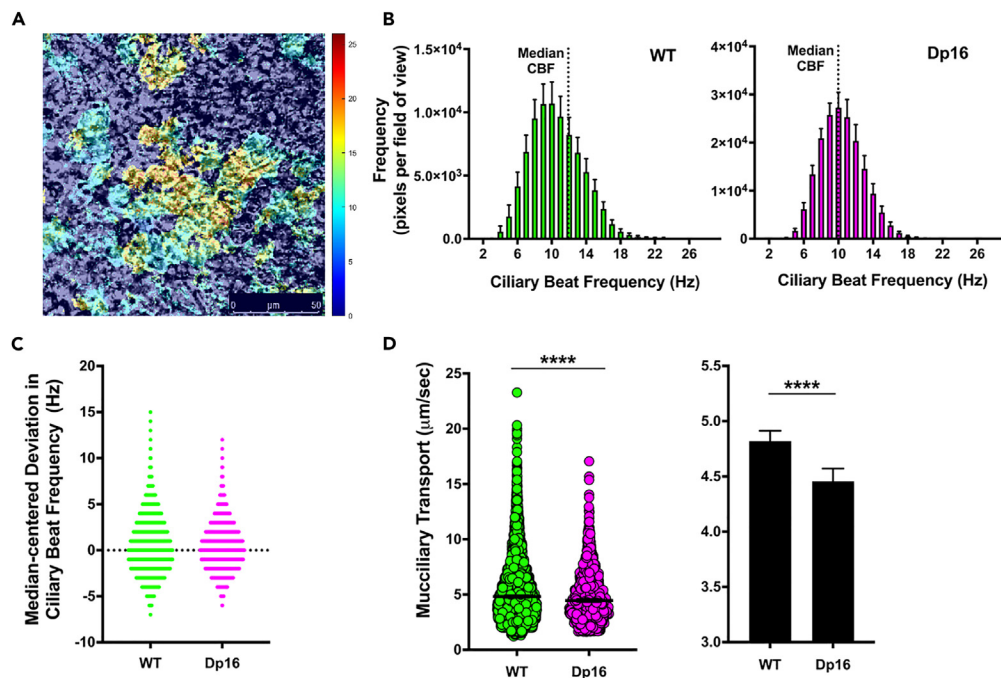


**Figure 2. T21 Leads to Altered Airway Motile Ciliary Function**

(A) Representative time-lapse heatmap of ciliary beat frequency (CBF) on the apical surface of the mTECs. Scale bar: 50 μm. Each code on the color table at right indicates a CBF.

(B) Profiles of CBF in WT and Dp16 mTECs. Data represents mean and s.e.m. from 2 to 5 fields of view (FOV) per replicate from three transwell inserts per condition ( $n = 8\text{--}13$  FOVs corresponding to 2,097,152–3,407,872 pixels). Note lower CBF median and range in Dp16 compared with WT mTECs.

(C) Spread of CBF expressed as deviation from median across both conditions. Note the skewness of the ciliary beatings.

(D) Mucociliary transport (MCT) on the luminal surface of WT and Dp16 mTECs was quantified utilizing nanobeads that were imaged at high frequency using a confocal microscope (Video S1). The two graphs illustrate the same data; the one on the left is scatter dot plot to show range and distribution of the MCT (μm/s) and the one on the right is a bar plot to exhibit differences in median MCT between the two conditions. Data represent median and 95% confidence interval of 3–5 FOAs per replicate from three biological replicates ( $n = 10\text{--}12$  corresponding to 1,638–6,793 individually captured MCT values; analyzed by non-parametric Mann-Whitney test). \*\* $p < 0.01$ , \*\*\*\* $p < 0.0001$ , n.s., not significant. Note the lower MCT in Dp16 vs. WT epithelia. See also Figure S3, and Video S1.

WT non-infected and Dp16 non-infected mTECs showed kurtosis values of  $-0.2389$  and  $0.1123$ , respectively; indicating that in WT epithelia most ciliary beatings occurred around the median, whereas in Dp16 epithelia there were more ciliary beatings in the distribution tails. Altogether, these data guided us to hypothesize that Dp16 mTECs compared with WT controls have reduced ability to clear inhaled (pathogenic and non-pathogenic) materials at homeostasis. So, we next analyzed mucociliary transport [MCT] by the mTECs using 200 nm fluorescent nanobeads (Video S1). We observed the MCT rate at WT epithelia is significantly higher than Dp16 mTECs ( $4.82$  vs.  $4.45$  μm/s median MCTs) (Figure 2D) validating our hypothesis.

### Immune response to influenza virus

Next, we analyzed the bulk RNA-seq data to further characterize baseline transcriptomic differences due to T21. Applying fast pre-ranked gene set enrichment analysis (fgSEA)<sup>11</sup> on Dp16 vs. WT (Table S1) using gene ontology (GO) biological process gene sets of the Molecular Signatures Database (MSigDB), we identified 433 gene sets (Table S2) that were significantly enriched (adjusted  $p < 0.05$ ). Ranking these based on normalized enrichment score (NES), we noticed that most of gene sets with the highest NES values pointed to immune pathways, inflammation, and defense response to other organisms (Tables S2 and S3, Figure 3A). Given the well documented impacts of immune dysregulation and lung infections in DS,<sup>1–5,7</sup> we then studied immune response to IAV infection in Dp16 and WT mTECs. We challenged the ciliated epithelia on D21 post-ALI with influenza virus strain A/Puerto Rico/8/1934 H1N1 (hereafter referred to as

**Table 1. Statistical Analyses on Ciliary Beat Frequency (CBF) from WT and Dp16 mTECs**

	WT	DP16
Minimum	3.000	3.000
25% Percentile	9.000	9.000
Median	12.00	10.00
75% Percentile	14.00	12.00
Maximum	27.00	25.00
Range	24.00	22.00
Skewness	0.3378	0.4552
Kurtosis	-0.2389	0.1123
<b>Test for Normal Distribution</b>		
<i>Anders on-Darling test</i>		
p value	<0.0001	<0.0001
Passes test	No	No
<i>D'Agostino &amp; Pears on test</i>		
p value	<0.0001	<0.0001
Passes test	No	No
<i>Kolmogorov-Smirnov test</i>		
p value	<0.0001	<0.0001
Passes test	No	No

IAV PR8) at representative multiplicity of infection (MOI) of 0.1 (Figure 3B), and quantified viral particles released from apical surface of the cells 48 h post-inoculation by real-time qPCR. Interestingly, we observed that both epithelia shed similar number of viral genomes (Figure 3C). We next performed bulk RNA-seq on IAV PR8-challenged mTECs along with their non-infected controls and analyzed coordinate pathway-level changes in the transcriptomic data to gain insight into gene sets that are significantly enriched upon viral infection in Dp16 and WT mTECs independently. For this analysis, we applied fgSEA and observed that 24 and 28 gene sets were significantly enriched (adjusted  $p < 0.05$ ) in WT and Dp16 mTECs, respectively, following infection with the influenza virus (Figure S4, Tables S4 and S5). Ranking the gene sets for each group based on NES revealed that the majority of induced pathways are immune related with IFN $\gamma$  response and IFN $\alpha$  response topping the list in both WT and Dp16 settings (Figures S4 and S5). Grossly evaluating genes in the IFN $\alpha$  response pathway in both WT and Dp16 epithelia (Figure S6; Table S6), via heatmap illustration of transcript levels, while clearly demonstrating a robust IFN signaling response, was insufficient to reveal differences in host response due to T21.

We then identified differentially expressed genes (DEGs) in 'Dp16 infected vs. Dp16 non-infected' comparison against 'WT infected vs. WT non-infected' (Table S7) and performed fgSEA as above on this list. We found there were five Hallmark gene sets that were significantly enriched, of which the most enriched one was 'TNF $\alpha$  signaling via NF- $\kappa$ B' (Figure 4A; Table S8). This strategy allowed us to better understand genes and pathways that may be differentially regulated upon infection in Dp16 mTECs compared with WT counterparts. We then plotted relative expression of several cytokines and chemokines (Cxcl1, Cxcl2, Cxcl5, Cxcl10, Cxcl11, Ccl12, Ccl20, Csf2, Il6, Tnf) from the 'TNF $\alpha$  signaling via NF- $\kappa$ B' pathway (Figure 4B; Table S9) and indeed observed a higher magnitude of immune responsiveness at the transcription level in Dp16 epithelia compared with WT upon influenza virus infection. Next, we evaluated secretion of CXCL2, IL6 and TNF (Figure 4C) as representative genes from Figure 4B and observed a similar pattern at protein level; however, as shown in Figure 4C the difference between the two epithelium types did not reach statistical significance. Taking a discovery approach and looking into whether other cytokines and chemokines may be differentially produced in Dp16 mTECs, we studied levels of several secreted pro-inflammatory proteins in the culture medium. Interestingly, we observed production of monocyte-recruiting chemokines CCL2, CCL3, CCL4 and CCL7 were either mildly induced or remained unchanged in WT mTECs following IAV PR8 infection, whereas they were considerably upregulated in Dp16 epithelial upon viral challenge (Figure 4C). In fact, the magnitude of induction in expression of these proteins was

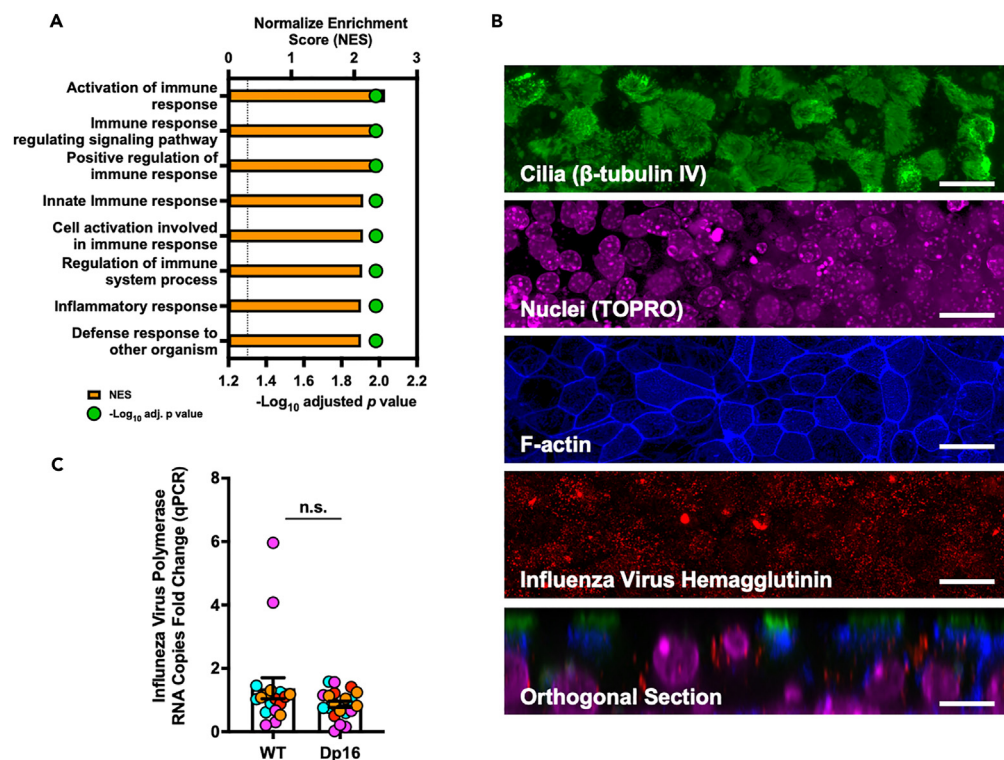


### Figure 3. Characterization of Influenza Viral Infection of Airway Epithelia in Down Syndrome *In Vitro*

(A) Fast Gene Set Enrichment Analysis (fGSEA) on differentially expressed genes (DEGs) in ‘Dp16 vs. WT’ (Table S1), by running against ‘Gene Ontology Biological Process’ pathways, identified enriched gene sets (Table S2) for involvement in immune pathways, inflammation, and defense response to other organisms. Representative gene sets with highest Normalized Enrichment Score (NES) are shown here (Table S3).

(B) Influenza A virus (IAV) challenge of *in vitro*-differentiated primary mTECs. Representative immunostaining images of ciliated mTECs from Dp16 Mice 48 h following challenge with IAV strain A/Puerto Rico/8/1934 H1N1 at MOI of 0.1. Individual markers for cilia (green;  $\beta$ -tubulin IV), nuclei (magenta; TO-PRO 3), cell-cell boundaries (blue; F-actin) and viral particles (red, hemagglutinin), as well as an orthogonal section as well as a top view of the infected cells are illustrated. Scale bar, 20  $\mu$ m (applies to all images).

(C) Real-time qPCR revealed comparable (statistically non-significant) influenza virus genome copies shed from infected WT and Dp16 mTECs; fold change in Dp16 vs. WT (as reference) is illustrated. Data represent mean and s.e.m. compared to WT from four independent studies (indicated by different coloring) with 3–6 biological replicates – i.e., transwell inserts, per condition (WT and Dp16) per study ( $n = 18\text{--}20 \times$  transwell inserts in total). Analysis was conducted by non-parametric Mann-Whitney test. n.s., not significant. See also Figures S4–S6 and Tables S1, S2, S3, S4, and S5.

significantly higher in Dp16 infected vs. WT infected mTECs. Next, we performed an *in vivo* study by which WT and Dp16 mice were challenged intranasally with IAV PR8. On day 6 post-infection we sacrificed the mice and analyzed cellular components of the bronchoalveolar lavage fluid (BALF) by flow cytometry (gating strategy is shown in Figure S1C) and studied virus shedding by qPCR (Figures 5A and 5B). In addition, we examined cytokines/chemokines in the BALF by multiplexed bead-based assays (Figure 5C). In line with our *in vitro* findings (Figure 4), we observed an immune hyperreactivity phenotype in Dp16 mice compared with WT controls, evidenced by statistically significant higher number of lung airway infiltrated monocytes, and elevated IFN $\gamma$  and CCL11 protein levels. There was also an increased trend with BALF neutrophil count, and CXCL10, IL6 and BAFF although these did not reach statistical significance. In our cytokine/chemokine analysis we studied over 40 analytes (see STAR Methods for details) of which only six were detectable (IFN $\gamma$ , CCL11, CXCL10, IL6, BAFF and CCL7); unfortunately, some values for CCL7 were missing and the data is not presented. The weight loss was comparable in both conditions (Figure S7).

## DISCUSSION

Given the scarcity and challenges of obtaining airway epithelial cells from people with DS, here, we isolated mTECs with high purity from lungs of WT and Dp16 mice, cultured *in vitro* and guided to terminal

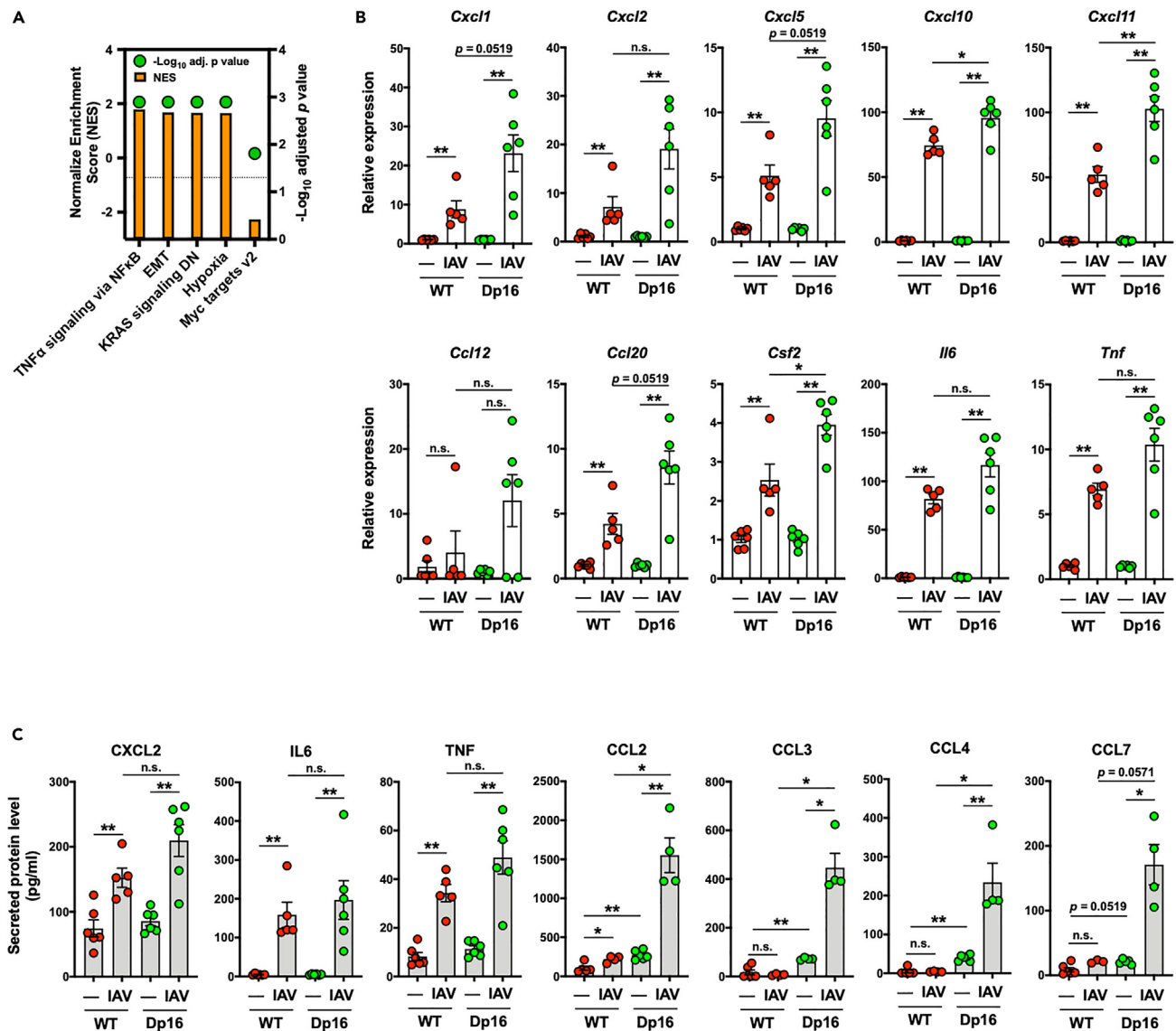


**Figure 4. Identification of Immune Hyperresponsiveness Phenotype to Influenza Infection in Ciliated Airway Epithelium Due to T21**

(A) fGSEA on DEGs in ‘Dp16 infected vs. Dp16 non-infected’ comparison against ‘WT infected vs. WT non-infected’ (Table S7), by running against ‘Hallmark’ pathways, identified five enriched gene sets which we ranked based on NES. The p value adjustment is against False Discovery Rate.

(B) Relative expression of select genes from the enriched ‘TNF $\alpha$  signaling via NF- $\kappa$ B’ gene list (Table S8) ( $n = 5\text{--}6 \times$  transwell inserts per group [WT and Dp16] per condition; analyzed by non-parametric Mann-Whitney test). Note the greater magnitude of upregulation in Dp16 epithelia.

(C) Secreted protein levels of cytokines and chemokines from non-infected and IAV-infected (48 h post-inoculation) WT and Dp16 mTECs ( $n = 4\text{--}6 \times$  transwell inserts per group [WT and Dp16] per condition; analyzed by non-parametric Mann-Whitney test). Note the similar trend in proteomic data as those observed for gene expression in (B). Data represent mean and s.e.m. \* $p < 0.05$ , \*\* $p < 0.01$ , n.s., not significant. See also Tables S7, S8, and S9.

differentiation into ciliated epithelia under ALI. We then characterized biology and function of the ciliated epithelia at homeostasis and following challenge with IAV. We discovered that Dp16 epithelia have significantly lower abundance of multiciliated cells in their tracheal epithelium in *in vitro* cultures. In addition, we identified altered ciliary function measurements in the trisomic epithelia. Specifically, we revealed that Dp16 compared with WT epithelia exhibit a narrower range of ciliary beating and lower CBF median. Moreover, we uncovered that mucociliary transport rate at Dp16 epithelia is significantly lower than WT mTECs. Interestingly, when challenged with IAV, both disomic and trisomic epithelia released similar quantities of viral particles following infection. However, RNA-sequencing, and proteomic analyses revealed an immune hyperreactive phenotype, particularly for monocyte-recruiting chemokines, in Dp16 epithelia. Importantly,

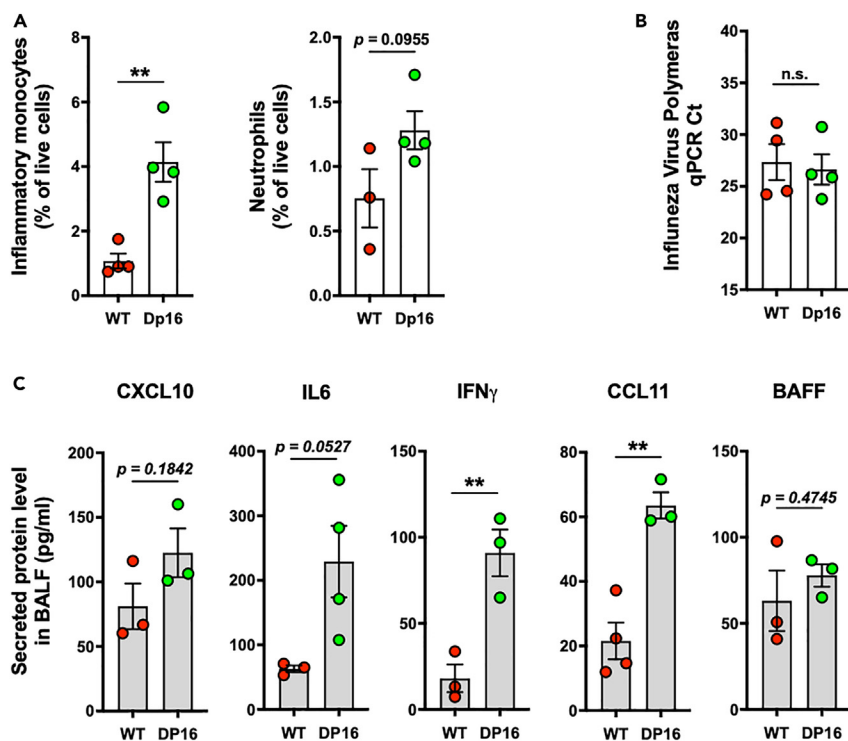


**Figure 5. In Vivo Confirmation of Immune Hyperresponsiveness Phenotype to Influenza Infection Due to T21**

(A) Flow cytometry analysis of lung airway infiltrated inflammatory monocytes (CD11b<sup>+</sup> Ly6C<sup>+</sup> Ly6G<sup>-</sup>) and neutrophils (CD11b<sup>+</sup> Ly6C<sup>+</sup> Ly6G<sup>+</sup>) in bronchoalveolar lavage fluid (BALF) of WT and Dp16 mice 6 days post-infection with IAV PR8. Note significant increase in inflammatory monocytes abundance and increased trend, albeit non-significant, in neutrophil increase in Dp16 mice compared with WT controls.

(B) Cycle of threshold (Ct) values from real-time qPCR on BALF for IAV polymerase genome were not statistically different, indicating comparable virus shedding consistent with our *in vitro* observation in Figure 4C.

(C) Secreted protein levels of cytokines and chemokines from IAV-infected (6 days post-inoculation) WT and Dp16 mice.  $n = 3-4 \times$  mice per group (WT and Dp16); data were analyzed by unpaired two-tailed Student's t test. \*\* $p < 0.01$ . See also Figure S7.

in line with our *in vitro* findings, when we challenged mice *in vivo* with IAV, we observed immune hyperresponsiveness in Dp16 mice evidenced by statistically significant higher number of lung airway infiltrated monocytes, and elevated IFN $\gamma$  and CCL11 protein levels.

Our findings on impact of DS on ciliated cells in mTECs are in line with earlier studies by Galati et al. who reported disruption of cilia formation and signaling due to T21.<sup>12</sup> The authors, however, studied primary (not motile) cilia and performed their studies on dermal fibroblasts (not lung airway epithelial cells).<sup>12</sup> Nevertheless, Galati et al., made the important finding that cilia defects arise from increased expression of pericentrin (PCNT) gene, a centrosome scaffold and trafficking protein encoded on human chr21. Notably, in our approach, it is unlikely that differential ciliary phenotypes can be attributed to pericentrin, as PCNT gene is encoded on murine chr10, which is not triplicated in Dp16 mice. In fact, a close look at genes differentially expressed in Dp16 vs. WT mTECs revealed no statistically significant change in expression of PCNT (Table S1).

In our studies, we found that extending epithelial cell culture *in vitro* up to D89 post-ALI did not change such difference in abundance of ciliated cells, implying that delayed differentiation is unlikely to explain this observation. In addition, to our surprise, we found that Dp16 ciliated cells have higher fluorescent signal intensity for  $\beta$ -tubulin IV – i.e., an indirect measure of cilia per cell, compared with WT counterparts (Figure S2). This implies that while Dp16 vs. WT mTECs have significantly lower number of ciliated cells, they appear to be partly correcting for this loss via increased number of cilia per cell. Notably, ultrastructural evaluation of clinical upper respiratory tract samples suggests lack of defect in architecture of cilia due

to T21.<sup>13</sup> On the other hand, the lower CBF in Dp16 mTECs is consistent with a clinical report by Piatti, et al. who in a study of 18 people with Down syndrome and 18 healthy controls found that CBF on nasal epithelial samples was lower in the DS group.<sup>13</sup>

Reduced MCT in Dp16 epithelia (Figure 2D) can be explained by lower ciliary beating capability (lower CBF median, lower CBF maximum value and shorter CBF range). Our observation on reduced ciliary beating ability in Dp16 mTECs is in line with two earlier studies.<sup>14,15</sup> Raveau et al., reported ependymal cilia beating deficiency in Ts1Rhr murine model of DS,<sup>14</sup> and Kogiso et al., found reduced basal CBF of airway cilia in Ts1Rhr mice.<sup>15</sup> The study by Raveau et al., while not lung airways, evaluated motile cilia which makes it relevant to our findings. On the other hand, the work by Kogiso et al., while informative, has a number of drawbacks compared to our studies: (1) relatively extensive tissue processing and dissociation was applied to obtain single cells (containing ciliated cells) from lungs prior to recording of CBF values *in vitro* (whereas we imaged the cells without perturbation), (2) isolated ciliated cells were placed on a coverslip within a microperfusion chamber – i.e., in a submerged state in culture media, for ciliary analysis (whereas we studied CBF under physiological ALI and without submerging the epithelia), (3) only 1–2 cells or a cell block per coverslip were analyzed (authors claim to have studied 4–10 coverslips from 2 to 5 animals) (whereas we studied all beating cells in each field of view (FOV) and evaluated multiple FOVs per biological replicate per condition [see STAR Methods]), and (4) CBF mean was compared between conditions without properly assessing normality of CBF distribution (whereas we first showed that data in WT and Dp16 mTECs are not normally distributed and then compared median, instead of mean, for statistical calculations). The measurable differences in CBF and MCT in Dp16 vs. WT mTECs may have implications for innate defense against inhaled particles, irritants, and pathogens. We postulate that the slightly lower, yet statistically significant, median ciliary beating and MCT rate in Dp16 may contribute to chronic pathologies associated with impaired mucociliary clearance such as cough, dyspnea, and recurring pulmonary infections. In support of this, it has been reported that children with DS show signs and symptoms associated with diffuse parenchymal lung disease such as chronic radiographic changes linked to dyspnea and cough.<sup>16</sup> Similarly, clinical evidence on recurrent pneumonias in people with trisomy 21 has been presented by multiple groups.<sup>17–20</sup>

Our experiments uncovered an immune hyperreactivity at the lung airway epithelium level to IAV infection due to T21, which is consistent with elevated responsiveness of human immune cells with T21 to Type I IFN,<sup>9</sup> and Dp16 immune cells to both Type I and II IFN ligands.<sup>21</sup> Moreover, significant induction of monocyte-recruiting chemokines in our studies may in part explain elevated levels of circulating intermediate (CD14<sup>+</sup> CD16<sup>+</sup>) and nonclassical (CD14<sup>-/dim</sup> CD16<sup>+</sup>) monocytes in DS<sup>9</sup> as secretion of CCL2, CCL3 and CCL4 from unchallenged mTECs is higher in Dp16 than the WT controls (Figure 4C).

In summary, our findings are first-in-kind to reveal an immune hyperresponsiveness phenotype to influenza virus in ciliated airway epithelium due to T21, and demonstrate differential CBF pattern, ciliated cell frequency in well-differentiated epithelia, and MCT at homeostasis. For future studies, it would be of great interest to recapitulate these findings using induced pluripotent stem cell (iPSC)-derived mucociliated human airway epithelia and/or nasal epithelia (which can be obtained by a minimally invasive brushing technique) from healthy subjects and individuals with DS (given the difficulties in obtaining lung tissue such as bronchial epithelial cells from people with T21), and culture these cells in microfluidic Organ-on-Chip devices such as Airway-on-a-Chip<sup>22</sup> to examine role of rhythmic breathing airflow to ciliary function in euploid cells and those with triplication of chr21, alone and in co-culture with lung microvascular endothelial cells and circulating/tissue-resident immune cells. Ultimately, such studies will shed light on biological processes that lead to recurrent respiratory infections in DS (both from an immune perspective and subsequent to pathogen retention due to differential ciliary expression and function) and what intervention modalities can be applied to mitigate such health risks.

### Limitations of the study

Overall, five limitations should be considered when evaluating our studies: (1) *in vivo* data on abundance of ciliated epithelial cells is missing, (2) our generated data are based on studies using animal-derived cells, (3) male and female mice were mixed based on availability and it is not possible to know the influence of sex on the results, (4) there is limited recreation of organ-level complexities and breathing-associated mechanical forces of the lungs, and (5) our statistical approach must be considered when examining our findings. Future studies on native trachea to characterize and confirm reduced frequency of multiciliated cells in Dp16 vs. WT mice is needed. In addition, utilizing a murine model like Dp16 can be a reasonable starting

point for mechanistic insight into DS and associated airway pathophysiology but given inter-species differences in translation of findings it is important that in future physiologically and clinically relevant endpoints be studied using human-derived cells. Moreover, while we focused on airway epithelium, future studies should incorporate additional organ-level complexities such as tissue-tissue crosstalk between mucociliated epithelia and pulmonary endothelium during inflammatory/immune response development, rhythmic breathing-associated airflow movements at homeostasis and during pathogen delivery, inclusion of circulating and/or resident immune cells, and communication with an immune organ (e.g., bone marrow or lymph node). These can be examined using Organ-on-a-Chip technology.<sup>22–32</sup> Lastly, to obtain  $n = 6$  transwell inserts, we sacrificed and combined tracheas from 3 to 5 mice during tissue dissociation so that adequate cells are present to differentiate *in vitro*, and when experiments were performed on independent sets of mice, they were clearly stated in figure legends. Appropriate statistical analysis approach based on the studied endpoint is discussed under Statistical Analysis in STAR Methods.

## STAR★METHODS

Detailed methods are provided in the online version of this paper and include the following:

- KEY RESOURCES TABLE
- RESOURCE AVAILABILITY
  - Lead contact
  - Materials availability
  - Data and code availability
- EXPERIMENTAL MODEL DETAILS
  - Animals
  - Cell isolation and culture
  - Influenza A virus
- METHOD DETAILS
  - Culture medium formulations
  - TEER measurement
  - In vitro virus infection
  - In vivo virus infection
  - Flow cytometry
  - Immunofluorescent staining and imaging
  - Cytokine and chemokine quantification
  - Viral RNA isolation, and real-time PCR analysis
  - Cellular RNA isolation, bulk sequencing and analysis
  - Luminex multiplex cytokine and chemokine assay
  - Ciliary beating frequency measurement
  - Mucociliary transport measurement
- QUANTIFICATION AND STATISTICAL ANALYSIS

## SUPPLEMENTAL INFORMATION

Supplemental information can be found online at <https://doi.org/10.1016/j.isci.2023.107361>.

## ACKNOWLEDGMENTS

**General:** We thank Mr. Ross Minter for breeding animals, Ms. Katrina Diener, Ms. Okyong Cho, Mr. Ted Shade and Dr. Bifeng Gao at University of Colorado Cancer Center Genomics Shared Resource Core for their assistance with sample preparation for RNA-seq, Dr. Eszter Vadar for discussions and troubleshooting murine epithelial cultures, Dr. Steven Brody for discussion on scRNA-seq data, Dr. Chad Pearson for discussions on ciliopathies, and staff at the Luminex Core Facility, University of Pittsburgh Cancer Institute, Hillman Cancer Center as well as the Colorado Cancer Center Flow Cytometry Shared Resource Core for their assistance with running the multiplexed cytokine/chemokine assay on Luminex system. The murine lung image in Figure 1 and part of Graphical Abstract were created with BioRender.com and exported under a paid subscription.

**Funding:** This work was supported by the Division of Pulmonary, Allergy and Critical Care Medicine at University of Pittsburgh (to K.H.B.), Linda Crnic Institute for Down Syndrome Grand Challenge Grant (to

K.H.B.), the Global Down Syndrome Foundation, the Anna and John J. Sie Foundation, National Institutes of Health Cancer Center Support Grant (P30CA046934) supporting the Bioinformatics and Biostatistics, Genomics and Flow Cytometry Shared Resource Cores, the CRIPT (Center for Research on Influenza Pathogenesis and Transmission), an NIAID-funded Center of Excellence for Influenza Research and Response (CEIRR, contract # 75N93021C00014), NIH grants R01HL159494 (to K.H.B.), U01EB029085 (to K.H.B.), U19AI142733 and U19AI135972 (to A.G-S.), and R01AI50305 from the NIH INCLUDE Project (to J.M.E).

## AUTHOR CONTRIBUTIONS

Conceptualization, K.H.B. Investigation, S.T., B.F.N., R.J.J-V., and R.C.A. Formal Analysis, K.H.B., S.T., B.F.N., R.J.J-V., A.J.K., and R.C.A. Software, A.J.K. Writing-Original Draft, K.H.B. Methodology, K.H.B., J.M.E., and K.D.S. Data curation, A.G. and J.C.C. Resources, A.G-S., and J.K.A. Writing – Review and Editing, K.H.B., J.M.E., K.D.S., and A.G-S. Supervision, K.H.B. Project Administration, K.H.B. Funding Acquisition, K.H.B.

## DECLARATION OF INTERESTS

K.H.B. is founder and holds equity in Pneumax, LLC. The A.G-S. laboratory has received research support from Pfizer, Senhwa Biosciences, Kenall Manufacturing, Avimex, Johnson & Johnson, Dynavax, 7 Hills Pharma, PharmaMar, ImmunityBio, Accurius, nanoComposix, Hexamer, N-fold LLC, Model Medicines, Atea Pharma, Applied Biological Laboratories, and Merck, outside of the reported work. A.G-S. has consulting agreements for the following companies involving cash and/or stock: Vivaldi Biosciences, ContraFect, 7 Hills Pharma, Avimex, Vaxalto, Pagoda, Accurius, Esperovax, Farmak, Applied Biological Laboratories, Pharmamar, Paratus, CureLab Oncology, CureLab Veterinary, Synairgen, and Pfizer, outside of the reported work. A.G-S. has been invited as speaker to meeting events organized by Sequirus, Janssen, and AstraZeneca. A.G-S. is inventor on patents and patent applications on the use of antivirals and vaccines for the treatment and prevention of virus infections and cancer, owned by the Icahn School of Medicine at Mount Sinai, New York, outside of the reported work.

Received: December 21, 2022

Revised: June 1, 2023

Accepted: July 10, 2023

Published: July 14, 2023

## REFERENCES

- Colvin, K.L., and Yeager, M.E. (2017). What people with Down Syndrome can teach us about cardiopulmonary disease. *Eur. Respir. Rev.* 26, 160098. <https://doi.org/10.1183/16000617.0098-2016>.
- Davidson, M.A. (2008). Primary care for children and adolescents with Down syndrome. *Pediatr. Clin.* 55, 1099–1111. <https://doi.org/10.1016/j.pcl.2008.07.001>.
- Garrison, M.M., Jeffries, H., and Christakis, D.A. (2005). Risk of death for children with down syndrome and sepsis. *J. Pediatr.* 147, 748–752. <https://doi.org/10.1016/j.jpeds.2005.06.032>.
- Hilton, J.M., Fitzgerald, D.A., and Cooper, D.M. (1999). Respiratory morbidity of hospitalized children with Trisomy 21. *J. Paediatr. Child Health* 35, 383–386. <https://doi.org/10.1046/j.1440-1754.1999.00386.x>.
- Clift, A.K., Coupland, C.A.C., Keogh, R.H., Hemingway, H., and Hippisley-Cox, J. (2021). COVID-19 Mortality Risk in Down Syndrome: Results From a Cohort Study Of 8 Million Adults. *Ann. Intern. Med.* 174, 572–576. <https://doi.org/10.7326/M20-4986>.
- De Lausnay, M., Verhulst, S., Boel, L., Wojciechowski, M., Boudewyns, A., and Van Hoorenbeeck, K. (2020). The prevalence of lower airway anomalies in children with Down syndrome compared to controls. *Pediatr. Pulmonol.* 55, 1259–1263. <https://doi.org/10.1002/ppul.24741>.
- Sullivan, K.D., Lewis, H.C., Hill, A.A., Pandey, A., Jackson, L.P., Cabral, J.M., Smith, K.P., Liggett, L.A., Gomez, E.B., Galbraith, M.D., et al. (2016). Trisomy 21 consistently activates the interferon response. *Elife* 5, e16220. <https://doi.org/10.7554/eLife.16220>.
- Sullivan, K.D., Evans, D., Pandey, A., Hraha, T.H., Smith, K.P., Markham, N., Rachubinski, A.L., Wolter-Warmerdam, K., Hickey, F., Espinosa, J.M., and Blumenthal, T. (2017). Trisomy 21 causes changes in the circulating proteome indicative of chronic autoinflammation. *Sci. Rep.* 7, 14818. <https://doi.org/10.1038/s41598-017-13858-3>.
- Waugh, K.A., Araya, P., Pandey, A., Jordan, K.R., Smith, K.P., Granrath, R.E., Khanal, S., Butcher, E.T., Estrada, B.E., Rachubinski, A.L., et al. (2019). Mass Cytometry Reveals Global Immune Remodeling with Multi-lineage Hypersensitivity to Type I Interferon in Down Syndrome. *Cell Rep.* 29, 1893–1908.e4. <https://doi.org/10.1016/j.celrep.2019.10.038>.
- Aziz, N.M., Guedj, F., Pennings, J.L.A., Olmos-Serrano, J.L., Siegel, A., Haydar, T.F., and Bianchi, D.W. (2018). Lifespan analysis of brain development, gene expression and behavioral phenotypes in the Ts1Cje, Ts65Dn and Dp(16)1/Yey mouse models of Down syndrome. *Dis. Model. Mech.* 11, dmm031013. <https://doi.org/10.1242/dmm.031013>.
- Subramanian, A., Tamayo, P., Mootha, V.K., Mukherjee, S., Ebert, B.L., Gillette, M.A., Paulovich, A., Pomeroy, S.L., Golub, T.R., Lander, E.S., and Mesirov, J.P. (2005). Gene set enrichment analysis: a knowledge-based approach for interpreting genome-wide expression profiles. *Proc. Natl. Acad. Sci. USA* 102, 15545–15550. <https://doi.org/10.1073/pnas.0506580102>.
- Galati, D.F., Sullivan, K.D., Pham, A.T., Espinosa, J.M., and Pearson, C.G. (2018). Trisomy 21 Represses Cilia Formation and Function. *Dev. Cell* 46, 641–650.e6. <https://doi.org/10.1016/j.devcel.2018.07.008>.
- Piatti, G., Allegra, L., Ambrosetti, U., and De Santi, M.M. (2001). Nasal ciliary function and

- ultrastructure in Down syndrome. *Laryngoscope* 111, 1227–1230. <https://doi.org/10.1097/00005537-200107000-00016>.
14. Raveau, M., Nakahari, T., Asada, S., Ishihara, K., Amano, K., Shimohata, A., Sago, H., and Yamakawa, K. (2017). Brain ventriculomegaly in Down syndrome mice is caused by Pcp4 dose-dependent cilia dysfunction. *Hum. Mol. Genet.* 26, 923–931. <https://doi.org/10.1093/hmg/ddx007>.
  15. Kogiso, H., Raveau, M., Yamakawa, K., Saito, D., Ikeuchi, Y., Okazaki, T., Asano, S., Inui, T., Marunaka, Y., and Nakahari, T. (2020). Airway Ciliary Beating Affected by the Pcp4 Dose-Dependent [Ca(2+)]i Increase in Down Syndrome Mice, Ts1Rhr. *Int. J. Mol. Sci.* 21, 1947. <https://doi.org/10.3390/ijms21061947>.
  16. McDowell, K.M., and Craven, D.I. (2011). Pulmonary complications of Down syndrome during childhood. *J. Pediatr.* 158, 319–325. <https://doi.org/10.1016/j.jpeds.2010.07.023>.
  17. Bloom, J.L., Frank, B., Weinman, J.P., Galambos, C., O’Leary, S.T., Liptzin, D.R., and Fuhlbrigge, R.C. (2021). Diffuse alveolar hemorrhage in children with trisomy 21. *Pediatr. Rheumatol. Online J.* 19, 114. <https://doi.org/10.1186/s12969-021-00592-4>.
  18. Bertrand, P., Navarro, H., Caussade, S., Holmgren, N., and Sánchez, I. (2003). Airway anomalies in children with Down syndrome: endoscopic findings. *Pediatr. Pulmonol.* 36, 137–141. <https://doi.org/10.1002/ppul.10332>.
  19. McLaughlin, F.J., Strieder, D.J., Harris, G.B., Vawter, G.P., and Eraklis, A.J. (1985). Tracheal bronchus: association with respiratory morbidity in childhood. *J. Pediatr.* 106, 751–755. [https://doi.org/10.1016/s0022-3476\(85\)80348-6](https://doi.org/10.1016/s0022-3476(85)80348-6).
  20. Chen, J., Ma, H., Zheng, Y., Cao, J., Zeng, H., and Zhang, Q. (2015). [Trisomy 21 syndrome associated interstitial lung disease: a case report]. *Zhonghua Er Ke Za Zhi* 53, 771–774.
  21. Tuttle, K.D., Minter, R., Waugh, K.A., Araya, P., Ludwig, M., Sempeck, C., Smith, K., Andrysik, Z., Burchill, M.A., Tamburini, B.A., et al. (2020). JAK1 inhibition blocks lethal sterile immune responses: implications for COVID-19 therapy. Preprint at bioRxiv. <https://doi.org/10.1101/2020.04.07.024455>.
  22. Benam, K.H., Villenave, R., Lucchesi, C., Varone, A., Hubeau, C., Lee, H.H., Alves, S.E., Salmon, M., Ferrante, T.C., Weaver, J.C., et al. (2016). Small airway-on-a-chip enables analysis of human lung inflammation and drug responses in vitro. *Nat. Methods* 13, 151–157. <https://doi.org/10.1038/nmeth.3697>.
  23. Benam, K.H., Burgess, J.K., and Stewart, A.G. (2021). Editorial: Accelerated Translation Using Microphysiological Organoid and Microfluidic Chip Models. *Front. Pharmacol.* 12, 827172. <https://doi.org/10.3389/fphar.2021.827172>.
  24. Benam, K.H., Dauth, S., Hassell, B., Herland, A., Jain, A., Jang, K.J., Karalis, K., Kim, H.J., MacQueen, L., Mahmoodian, R., et al. (2015). Engineered in vitro disease models. *Annu. Rev. Pathol.* 10, 195–262. <https://doi.org/10.1146/annurev-pathol-012414-040418>.
  25. Benam, K.H., Gilchrist, S., Kleensang, A., Satz, A.B., Willett, C., and Zhang, Q. (2019). Exploring new technologies in biomedical research. *Drug Discov. Today* 24, 1242–1247. <https://doi.org/10.1016/j.drudis.2019.04.001>.
  26. Benam, K.H., and Ingber, D.E. (2016). Commendation for Exposing Key Advantage of Organ Chip Approach. *Cell Syst.* 3, 411. <https://doi.org/10.1016/j.cels.2016.11.009>.
  27. Benam, K.H., Königshoff, M., and Eickelberg, O. (2018). Breaking the In Vitro Barrier in Respiratory Medicine. Engineered Microphysiological Systems for Chronic Obstructive Pulmonary Disease and Beyond. *Am. J. Respir. Crit. Care Med.* 197, 869–875. <https://doi.org/10.1164/rccm.201709-1795PP>.
  28. Benam, K.H., Mazur, M., Choe, Y., Ferrante, T.C., Novak, R., and Ingber, D.E. (2017). Human Lung Small Airway-on-a-Chip Protocol. *Methods Mol. Biol.* 1612, 345–365. [https://doi.org/10.1007/978-1-4939-7021-6\\_25](https://doi.org/10.1007/978-1-4939-7021-6_25).
  29. Benam, K.H., Novak, R., Ferrante, T.C., Choe, Y., and Ingber, D.E. (2020). Biomimetic smoking robot for in vitro inhalation exposure compatible with microfluidic organ chips. *Nat. Protoc.* 15, 183–206. <https://doi.org/10.1038/s41596-019-0230-y>.
  30. Benam, K.H., Novak, R., Nawroth, J., Hirano-Kobayashi, M., Ferrante, T.C., Choe, Y., Prantil-Baun, R., Weaver, J.C., Bahinski, A., Parker, K.K., and Ingber, D.E. (2016). Matched-Comparative Modeling of Normal and Diseased Human Airway Responses Using a Microengineered Breathing Lung Chip. *Cell Syst.* 3, 456–466.e4. <https://doi.org/10.1016/j.cels.2016.10.003>.
  31. Jimenez-Valdes, R.J., Can, U.I., Niemeyer, B.F., and Benam, K.H. (2020). Where We Stand: Lung Organotypic Living Systems That Emulate Human-Relevant Host-Environment/Pathogen Interactions. *Front. Bioeng. Biotechnol.* 8, 989. <https://doi.org/10.3389/fbioe.2020.00989>.
  32. Niemeyer, B.F., Zhao, P., Tuder, R.M., and Benam, K.H. (2018). Advanced Microengineered Lung Models for Translational Drug Discovery. *SLAS Discov.* 23, 777–789. <https://doi.org/10.1177/2472555218760217>.
  33. You, Y., Richer, E.J., Huang, T., and Brody, S.L. (2002). Growth and differentiation of mouse tracheal epithelial cells: selection of a proliferative population. *Am. J. Physiol. Lung Cell Mol. Physiol.* 283, L1315–L1321. <https://doi.org/10.1152/ajplung.00169>.
  34. Schoch, K.G., Lori, A., Burns, K.A., Eldred, T., Olsen, J.C., and Randell, S.H. (2004). A subset of mouse tracheal epithelial basal cells generates large colonies in vitro. *Am. J. Physiol. Lung Cell Mol. Physiol.* 286, L631–L642. <https://doi.org/10.1152/ajplung.00112.2003>.
  35. Lam, H.C., Choi, A.M.K., and Ryter, S.W. (2011). Isolation of Mouse Respiratory Epithelial Cells and Exposure to Experimental Cigarette Smoke at Air Liquid Interface. *JoVE*, e2513. <https://doi.org/10.3791/2513>.
  36. Vladar, E.K., and Brody, S.L. (2013). Chapter Fourteen - Analysis of Ciliogenesis in Primary Culture Mouse Tracheal Epithelial Cells. In *Methods in Enzymology*, W.F. Marshall, ed. (Academic Press), pp. 285–309. <https://doi.org/10.1016/B978-0-12-397944-5.00014-6>.
  37. You, Y., and Brody, S.L. (2013). Culture and Differentiation of Mouse Tracheal Epithelial Cells. In *Epithelial Cell Culture Protocols*, Second Edition, S.H. Randell and M.L. Fulcher, eds. (Humana Press), pp. 123–143. [https://doi.org/10.1007/978-1-62703-125-7\\_9](https://doi.org/10.1007/978-1-62703-125-7_9).
  38. Eenjes, E., Mertens, T.C.J., Buscop-van Kempen, M.J., van Wijck, Y., Taube, C., Rottier, R.J., and Hiemstra, P.S. (2018). A novel method for expansion and differentiation of mouse tracheal epithelial cells in culture. *Sci. Rep.* 8, 7349. <https://doi.org/10.1038/s41598-018-25799-6>.
  39. Uccellini, M.B., and García-Sastre, A. (2018). ISRE-Reporter Mouse Reveals High Basal and Induced Type 1 IFN Responses in Inflammatory Monocytes. *Cell Rep.* 25, 2784–2796.e3. <https://doi.org/10.1016/j.celrep.2018.11.030>.
  40. Niemeyer, B.F., Miller, C.M., Ledesma-Feliciano, C., Morrison, J.H., Jimenez-Valdes, R., Clifton, C., Poeschla, E.M., and Benam, K.H. (2022). Broad antiviral and anti-inflammatory efficacy of nafamostat against SARS-CoV-2 and seasonal coronaviruses in primary human bronchiolar epithelia. *Nano Sel.* 3, 437–449. <https://doi.org/10.1002/nano.202100123>.
  41. Niemeyer, B.F., and Benam, K.H. (2022). Untapping host-targeting cross-protective efficacy of anticoagulants against SARS-CoV-2. *Pharmacol. Ther.* 233, 108027. <https://doi.org/10.1016/j.pharmthera.2021.108027>.
  42. Cho, J.L., Roche, M.I., Sandall, B., Brass, A.L., Seed, B., Xavier, R.J., and Medoff, B.D. (2012). Enhanced Tim3 activity improves survival after influenza infection. *J. Immunol.* 189, 2879–2889. <https://doi.org/10.4049/jimmunol.1102483>.
  43. Bushnell, B. (2020). BBMap: BBMap short read aligner, and other bioinformatic tools. <https://sourceforge.net/projects/bbmap/>.
  44. Dobin, A., Davis, C.A., Schlesinger, F., Drenkow, J., Zaleski, C., Jha, S., Batut, P., Chaisson, M., and Gingeras, T.R. (2013). STAR: ultrafast universal RNA-seq aligner. *Bioinformatics* 29, 15–21. <https://doi.org/10.1093/bioinformatics/bts635>.
  45. Robinson, M.D., McCarthy, D.J., and Smyth, G.K. (2010). edgeR: a Bioconductor package for differential expression analysis of digital gene expression data. *Bioinformatics* 26,

- 139–140. <https://doi.org/10.1093/bioinformatics/btp616>.
46. Ritchie, M.E., Phipson, B., Wu, D., Hu, Y., Law, C.W., Shi, W., and Smyth, G.K. (2015). limma powers differential expression analyses for RNA-sequencing and microarray studies. *Nucleic Acids Res.* 43, e47. <https://doi.org/10.1093/nar/gkv007>.
47. Sergushichev, A.A. (2019). Fast Gene Set Enrichment Analysis.
48. Liberzon, A., Subramanian, A., Pinchback, R., Thorvaldsdóttir, H., Tamayo, P., and Mesirov, J.P. (2011). Molecular signatures database (MSigDB) 3.0. *Bioinformatics* 27, 1739–1740. <https://doi.org/10.1093/bioinformatics/btr260>.
49. Gu, Z., Eils, R., and Schlesner, M. (2016). Complex heatmaps reveal patterns and correlations in multidimensional genomic data. *Bioinformatics* 32, 2847–2849. <https://doi.org/10.1093/bioinformatics/btw313>.
50. Schindelin, J., Arganda-Carreras, I., Frise, E., Kaynig, V., Longair, M., Pietzsch, T., Preibisch, S., Rueden, C., Saalfeld, S., Schmid, B., et al. (2012). Fiji: an open-source platform for biological-image analysis. *Nat. Methods* 9, 676–682. <https://doi.org/10.1038/nmeth.2019>.
51. Tinevez, J.Y., Rueden, C., and Eglinger, J. (2020). TrackMate-TrackAnalysis: Basic track analysis, plugged as TrackMate modules. <https://github.com/tinevez/TrackMate-TrackAnalysis>.

STAR★METHODS

KEY RESOURCES TABLE

REAGENT or RESOURCE	SOURCE	IDENTIFIER
<b>Antibodies</b>		
β-tubulin IV antibody (clone ONS.1A6)	GenTex	Cat# GTX11315; RRID: AB_373247
Keratin 5 antibody (clone Poly9059)	Biolegend	Cat# 905901; RRID: AB_2565054
FITC-conjugated goat anti-mouse IgG	Biolegend	Cat# 405305; RRID: AB_315008
Alexa Fluor Plus 594-conjugated goat anti-chicken IgY	Thermo Fisher	Cat# A32759; RRID: AB_2762829
CD11b-APC (M1/70)	BD	Cat# 553312; RRID: AB_398535
Ly6G-PE (1A18)	BD	Cat # 551461; RRID: AB_394208
Ly6C-FITC (AL-21)	BD	Cat# 553104; RRID: AB_394628
Anti-acetylated tubulin (clone 6-11B-1)	Sigma	Cat# T7451; RRID: AB_609894
Anti-influenza hemagglutinin (rabbit polyclonal IgG)	GenTex	Cat# GTX127357; RRID: AB_2728683
Alexa Fluor 568-conjugated goat anti-rabbit IgG	Thermo Fisher	Cat# A-11011; RRID: AB_143157
TO-PRO 3 Iodide	Thermo Fisher	Cat# T3605
Phalloidin-iFluor 405 (F-actin)	Abcam	Cat# ab176752
<b>Bacterial and virus strains</b>		
A/Puerto Rico/8/1934 H1N1 (IAV PR8)	ATTC	ATTC VR-1469™
<b>Chemicals, peptides, and recombinant proteins</b>		
Pronase	Roche	Cat# 10165913103
all-trans retinoic acid	Sigma	Cat# R2625
Y-27632 hydrochloride	Sigma	Cat# SCM075
Insulin	Sigma	Cat# I1882
Epidermal growth factor	BD Bioscience	Cat# 354001
NuSerum	BD Bioscience	Cat# 355504
<b>Critical commercial assays</b>		
Immune Monitoring 48-Plex Mouse ProcartaPlex™ Panel	Thermo Fisher	Cat. # EPX480-20834-901
QIAamp Viral RNA Lysis kit	Qiagen	Cat. # 52906
SuperScript™ III Reverse Transcriptase	Thermo Fisher	Cat# 18080093
iTaq™ Universal SYBR® Green Supermix	Bio-Rad	Cat# 1725120
RNeasy Mini Kit	Qiagen	Cat# 74104
Immune Monitoring 48-Plex Mouse ProcartaPlex™ Panel	Thermo Fisher	Cat# EPX480-20834-901
<b>Deposited data</b>		
Raw and processed bulk RNA sequencing data	This paper	GEO: GSE198902
<b>Experimental models: Organisms/strains</b>		
Mouse: Dp(16Lipi-Zbtb21)1Yey/J (Dp(16)1/Yey; Dp16)	The Jackson Laboratory	JAX: 013530; RRID: IMSR_JAX:013530
<b>Oligonucleotides</b>		
Random primers	Thermo Fisher	Cat. # 4819011
Primers directed against polymerase genomic segment: Forward: 5'- CGGTCCAAATTCCTGCTGA -3', Reverse: 5'- CATTGGGTTCTCCATCCA -3'	Cho et al. <sup>42</sup>	N/A
<b>Software and algorithms</b>		
FlowJo v10.7	BD	<a href="https://www.flowjo.com/">https://www.flowjo.com/</a> RRID:SCR_008520

(Continued on next page)

**Continued**

REAGENT or RESOURCE	SOURCE	IDENTIFIER
FIJI Trackmate	Schindelin et al. <sup>50</sup>	<a href="https://imagej.net/plugins/trackmate/">https://imagej.net/plugins/trackmate/</a>
TrackAnalysis	Tinevez et al. <sup>51</sup>	<a href="https://github.com/tinevez/TrackMate-TrackAnalysis">https://github.com/tinevez/TrackMate-TrackAnalysis</a>
BBDuk	BBDuk <sup>44</sup>	RRID:SCR_016969
STAR (2.6.0a)	Dobin et al. <sup>44</sup>	<a href="https://code.google.com/archive/p/rna-star/">https://code.google.com/archive/p/rna-star/</a> RRID:SCR_004463
fgSEA R package (v1.10.0)	Sergushichev <sup>47</sup>	<a href="https://bioconductor.org/packages/release/bioc/html/fgsea.html">https://bioconductor.org/packages/release/bioc/html/fgsea.html</a> RRID:SCR_020938
Molecular Signatures Database	Liberzon <sup>48</sup>	<a href="https://www.gsea-msigdb.org/gsea/msigdb">https://www.gsea-msigdb.org/gsea/msigdb</a> RRID:SCR_016863
ComplexHeatmap	Gu et al. <sup>49</sup>	<a href="https://bioconductor.org/packages/release/bioc/html/ComplexHeatmap.html">https://bioconductor.org/packages/release/bioc/html/ComplexHeatmap.html</a> RRID:SCR_017270

**Other**

FluoSpheres™ Carboxylate-Modified Microspheres	Thermo Fisher	Cat# F8811
--	---------------	------------

**RESOURCE AVAILABILITY**

**Lead contact**

Further information and requests for resources and reagents should be directed to and will be fulfilled by the lead contact, Kambez H. Benam ([benamk@pitt.edu](mailto:benamk@pitt.edu)).

**Materials availability**

This study did not generate new unique reagents.

**Data and code availability**

- Raw and processed bulk RNA-sequencing data are deposited in Gene Expression Omnibus under accession number GSE198902.
- This paper does not report original code.
- Any additional information required to reanalyze the data reported in this paper is available from the [lead contact](#) upon reasonable request.

**EXPERIMENTAL MODEL DETAILS**

**Animals**

Male and female mice from 6-8-week-old (mixed based on availability), used throughout the study were Dp(16Lipi-Zbtb21)1Yey/J (Dp(16)1Yey; Dp16) maintained on a C57BL/6J background (stock#013530; Jackson Laboratories). Mice were supplied through collaboration with the Espinosa Lab in the University of Colorado Denver Department of Pharmacology in conjunction with the Linda Crnic Institute for Down Syndrome. All mice were bred in-house at the University of Colorado Anschutz Medical Campus and were a kind gift through Sullivan and Espinosa Labs. Animal studies were approved by the Institutional Animal Care and Use Committee of University of Colorado Anschutz Medical Campus, and we complied with all relevant ethical regulations.

**Cell isolation and culture**

The Murine Tracheal Epithelial Cell (mTEC) cultures were generated through isolation, expansion, and differentiation of primary epithelial cells (male and female mixed based on availability) as previously described<sup>33–38</sup> with a few modifications. To obtain n = 6 transwell inserts, we sacrificed and combined tracheas from 3 to 5 mice (per Dp16 and WT) during tissue dissociation so that adequate cells are present to differentiate *in vitro*. In brief, mice were sacrificed humanely via inhalation of isoflurane (Sigma) and were sprayed thoroughly with 70% ethanol (EtOH) (Sigma). Tracheas were harvested from above larynx to below the tracheal bifurcation and placed into ice-cold Ham's F-12 culture medium supplemented with P/S (100 U/mL; 100 µg/mL). Each trachea was then carefully cleaned in a dish of 4°C-cold phosphate buffered

saline (PBS) (Sigma) before being cut open longitudinally and placed into a 15-mL conical tube containing 10 mL of Ham's-F12 supplemented with pronase (1.5 mg/mL) (Roche) and P/S (100 U/mL; 100 µg/mL). The tracheas were then digested overnight (18-24h) at 4°C. The tubes were inverted 10 times, 1 mL of FBS was added to each (to halt enzymatic digestion) and inverted for additional 12 times. Next, tracheas were transferred to a 15-mL conical containing 5 mL of Ham's F-12 supplemented with P/S (100 U/mL; 100 µg/mL) and FBS (10% v/v), inverted 12 times, and residual undigested tracheal tissue was removed and discarded. The dissociated cells in the suspension were spun down by centrifugation at 400 × g for 10 minutes at room temperature. The cells were then re-suspended in 1 mL of FBS and plated onto a Primaria™ Cell Culture Dish (Corning) containing 9 mL of mTEC Basic Medium. Plates were incubated at 37°C for 3.5–4 hours to allow for fibroblast attachment. Thus, epithelial cells remained unattached in the plate medium, and were collected, spun down, and re-suspended in mTEC Proliferation Medium supplemented with all-*trans* retinoic acid (ATRA; 50 nM) (Sigma) and Rho-associated protein kinase (ROCK) inhibitor Y-27632 hydrochloride (10 µM) (Sigma). mTECs were plated onto 0.4 µm transwell inserts (TWIs) (Corning) in a 24 well plate at approximately 41,000 cells/insert. In our studies, combining tracheas from a five-mouse harvest yielded approximately 500,000 cells allowing us to generate 12 × TWIs successfully. The cells expanded (on TWI) at 37°C, 5% CO<sub>2</sub> in humidified chamber (Thermo Fisher) for two days before medium was changed and TEER measurements could begin. By day 5 post-seeding cells were confluent and ready for ALI induction, and the cultures were maintained with 500 µL of mTEC ALI Medium in the basal chamber, with the medium was replaced every two days.

### Influenza A virus

All viral challenges were performed using influenza strain A/Puerto Rico/8/1934 H1N1 (IAV PR8) (ATCC).

## METHOD DETAILS

### Culture medium formulations

Culture Media were formulated based on previously published protocols.<sup>33–37</sup> mTEC Basic Medium consisted of 1:1 DMEM/F12 (Thermo Fisher) ratio supplemented with penicillin-streptomycin (P/S; 100 U/mL; 100 µg/mL) (Thermo Fisher) and NaHCO<sub>3</sub> (0.03% v/v) (Thermo Fisher). mTEC Proliferation Medium consisted of mTEC Basic Medium supplemented with insulin (10 µg/mL) (Sigma), epidermal growth factor (25 ng/mL) (BD Bioscience), apo-transferrin (5 µg/mL) (Sigma), cholera toxin (0.1 µg/mL) (Sigma), fetal bovine serum (FBS; 5% v/v) (Sigma), and bovine pituitary extract (0.03 mg/mL) (Sigma) in addition to all-*trans* retinoic acid (ATRA; 50 nM) (Sigma) and Rho-associated protein kinase (ROCK) inhibitor Y-27632 hydrochloride (10 µM) (Sigma) to enhance cellular proliferation.<sup>38</sup> ATRA and ROCK inhibitor were added fresh at each medium change. Once cells become fully confluent (in culture with mTEC Proliferation Medium), an air-liquid interface (ALI) was initiated, and mTEC ALI Medium was utilized to guide ciliary differentiation over a course of 14–21 days. The mTEC ALI Medium comprised of MTEC Basic Medium supplement fresh with ATRA (50nM) and NuSerum (2% v/v) (BD Bioscience).

### TEER measurement

Trans-epithelial electrical resistance (TEER) measurements were taken on a representative number of cultures starting at two days post-seeding. During cell proliferation, TEER measurements were taken daily and used as an indicator for initiation of ALI. Epithelial Volt/Ohm (TEER) Meter with STX3 (World Precision Instruments) electrodes were used to measure the electrical resistance across the cell monolayer. 200 µL of fully supplemented medium mTEC Proliferation or mTEC ALI was added into each apical chamber of each TWI and allowed to incubate at 37°C. After 10 minutes STX3 electrodes were positioned between the apical and basal chambers and raw measurements (Ω) were recorded. Apical media was then removed (when cultures in ALI) or exchanged for fresh media (culture in proliferation) and returned to culture. The resistance was then corrected for surface area.

### In vitro virus infection

Once mTEC cultures were fully confluent and well-differentiated (ALI day 21 or later)<sup>37</sup> cells were infected at multiplicity of infection (MOI) of 0.1 with IAV PR8 diluted in mTEC Basic Medium supplemented with ATRA. Viral inoculum was added to the apical chamber of each transwell (into the insert and over the luminal surface ciliated mTECs) at 200 µl inoculum per insert. The cells were then incubated for two hours at 35°C to allow adsorption of virus to the cells. After 2 hours, the inoculum was removed and TWIs were washed once with 200 µl of mTEC Basic Medium and the infected cells were returned to culture at 37°C, 5% CO<sub>2</sub> in a

humidified chamber. 48 hrs post-inoculation, 200  $\mu$ l of mTEC Basic Medium was added to the apical compartment of TWIs and cells were incubated for 10 minutes at 37°C. The apical washes were then collected to quantify virus shedding by quantitative real-time PCR (qPCR) analysis. When investigating secreted cytokines/chemokines, basal culture media from were collected and stored at  $-80^{\circ}\text{C}$  for future analysis.

### In vivo virus infection

6-10 weeks old female B6.129S7-Dp(16Lipi-Zbtb21)1Yey/J (Dp16) mice (stock#013530; Jackson Laboratories) were used in this study along non-carrier mice that were used as controls. Mice were anesthetized with ketamine/xylazine (95 mg/kg ketamine and 10 mg/kg xylazine) and infected intranasally with 30  $\mu$ l PBS containing  $10^4$  PFU of IAV PR8 virus as previously described.<sup>39</sup> Animal studies were approved by the Institutional Animal Care and Use Committee of Icahn School of Medicine at Mount Sinai, and we complied with all relevant ethical regulations. Mice were housed in a pathogen-free barrier facility and maintained with food and water *ad libitum*. At day 6 post-infection mice were humanely euthanized and lung airway washes for collection of cellular and non-cellular bronchoalveolar lavage fluid (BALF) was performed in 3 mL pf PBS. Cellular fractions were used immediately for flow cytometry analysis and the non-cellular fractions were stored at  $-80^{\circ}\text{C}$  for further cytokine/chemokine analysis.

### Flow cytometry

Quantitative distribution of epithelial subtypes was studied by flow cytometry. In our studies the two predominant epithelial subtypes present were ciliated and basal cells. After apical washes with PBS, the cells were detached from TWIs using 0.25% Trypsin EDTA (Thermo Fisher) by incubating at 37°C for 15 minutes. Samples were then fixed in paraformaldehyde (PFA; Electron Microscopy Science) in PBS (1% v/v), and permeabilized for intracellular staining using freshly prepared flow blocking buffer (FBS [5% v/v], BSA [1% w/v] [Thermo Fisher], saponin [0.1% w/v] [EMD Millipore] in PBS) for 1 hour at room temperature. Mouse-on-mouse endogenous binding was blocked by ReadyProbes™ Mouse-on-Mouse IgG Blocking Solution (Thermo Fisher) following manufacturer's instructions. The fixed, permeabilized cells were next co-stained for ciliated cells with  $\beta$ -tubulin IV antibody (clone ONS.1A6, GenTex), and basal cells with Keratin 5 antibody (clone Poly9059, Biolegend) followed by a secondary staining with FITC-conjugated goat anti-mouse IgG (Biolegend) and Alexa Fluor Plus 594-conjugated goat anti-chicken IgY (Thermo Fisher). The samples were immediately run on BD™ LSR II flow cytometer made available through the University of Colorado Anschutz Medical Campus Clinical Immunology Flow Cytometry/cell sorting core and at Dr. Benam's laboratory. Data was exported and processed using FlowJo v10.7.

Cellular components of BALF from mice at day 6 post-infection were resuspended in FACS buffer (PBS 1% BSA 0.5 mM EDTA). Cells were stained with CD11b-APC (M1/70), Ly6G-PE (1A18) and Ly6C-FITC (AL-21) antibodies (BD) in the presence of Fc-block reagent (BD) and fixable viability dye eFluor450 (eBioscience) for 20 min at 4°C. Cells were then fixed for 15 min with 4% formaldehyde (Electron Microscopy Science) following staining, samples were washed, resuspended in 300  $\mu$ l of FACS buffer, and analyzed using a Gallios cytometer (Beckman). Data was exported and processed using FlowJo v10.7.

### Immunofluorescent staining and imaging

The mTEC culture on TWIs were fixed with PFA (4% v/v in PBS) at 37°C for 15 min, followed by permeabilization with Triton X-100 solution (0.2% in PBS) (VWR) for 2 hrs at room temperature. Non-specific binding sites were blocked using immunofluorescent microscopy blocking buffer (BB) composed of FBS (5% v/v) and BSA (1% w/v) in PBS. Similar to flow cytometry analysis, mouse-on-mouse endogenous binding was blocked using ReadyProbes™ Mouse-on-Mouse IgG Blocking Solution diluted to in PBS (1% v/v). Next, the cultures were incubated with primary antibodies (anti- $\beta$ -tubulin IV [clone ONS.1A6, GeneTex], anti-acetylated tubulin [clone 6-11B-1, Sigma], anti-influenza hemagglutinin [rabbit polyclonal IgG, GeneTex]) for 1 hr at room temperature followed by incubation for secondary antibodies (FITC-conjugated goat anti-mouse IgG [Thermo Fisher], Alexa Fluor 568-conjugated goat anti-rabbit IgG [Thermo Fisher]), nuclear staining (TO-PRO 3 Iodide; Thermo Fisher) and F-actin (Abcam) for 45 min at room temperature in dark. The TWI membranes were then gently cut of the inserts using a scalpel and mounted onto glass slides for imaging. Multiple Z-Stacks were acquired using confocal imaging on a Leica TCS SPE DMI8 confocal microscope equipped with Hamamatsu ORCA-Flash4.0 V3 Digital CMOS camera and 63 $\times$  oil immersion objective.

For cilia count analysis, cell boundary and cilia immunostaining were performed as described above. The per-cell mean fluorescence intensity (MFI) of cilia was determined using the LAS X software (Leica). Briefly, cells were converted to regions of interest by creating a mask using the F-actin boundary stain. For the mask, the F-actin signal was inverted, and the option "fill holes" was selected as a binary process pre-filter. This process converted cells into objects without manually drawing regions of interest. The MFI of the cilia channel was then measured on each object with the minimum threshold set to 6. Only objects with an MFI >6.0 were counted as positive for cilia and were subsequently counted in MFI analysis.

### Cytokine and chemokine quantification

BALF washes from WT and Dp16 mice at 6 days post-infection were collected and used for cytokine, chemokine analysis. Quantification was performed on 50 µl of the media using Immune Monitoring 48-Plex Mouse ProcartaPlex™ Panel (Thermo Fisher Scientific, Cat. # EPX480-20834-901). This kit contained needed reagents for detection of these analytes: BAFF, CSF1, CSF2, CSF3, IFN $\alpha$ , IFN $\gamma$ , IL1 $\alpha$ , IL1 $\beta$ , IL2, IL3, IL4, IL5, IL6, IL7, IL9, IL10, IL12p70, IL13, IL15/IL15R, IL17A, IL18, IL19, IL-22, IL23, IL25, IL27, IL28, IL31, IL33, LIF, RANKL, TNF $\alpha$ , CXCL5, CCL11, CXCL1, CXCL10, CCL2, CCL3, CCL4, CCL5, CCL7, MIP-2, Betacellulin, Leptin, VEGFA, IL2R, IL7R $\alpha$ , IL33R. The measurement and analysis were performed using the UPMC Cancer Biomarkers Facility: Luminex Core Laboratory.

### Viral RNA isolation, and real-time PCR analysis

Viral RNA was isolated, and qPCR performed as previously described for coronaviruses<sup>40,41</sup> except that IAV PR8 primers were used instead. In brief, viral RNA was collected by mixing 140 µl of BALF with 560 µl of buffer AVL from QIAamp Viral RNA Lysis kit (Qiagen). RNA isolation proceeded according to the manufacturer's instructions. After RNA isolation, cDNA was generated using from 5 µl of RNA template using SuperScript™ III Reverse Transcriptase (Thermo Fisher) and random primers (Thermo Fisher). Quantification of IAV PR8 was performed using qRT-PCR using iTaq™ Universal SYBR® Green Supermix (Bio-Rad) using primers directed against polymerase genomic segment: Forward: 5'- CGGTCCAAATTCCTGCTGA -3', Reverse: 5'- CATTGGGTTCCCTCCATCCA -3', adapted from a prior report<sup>423</sup>.

### Cellular RNA isolation, bulk sequencing and analysis

Cells were lysed and RNA was extracted using RNeasy Mini Kit (Qiagen) following the manufacturer instructions. In short, cell lysates were collected and placed into specialized columns in which DNA is eliminated before the remaining RNA was thoroughly washed with a specific sequence of buffers. Finally, the RNA was eluted from the column membrane and transferred into 1.5 mL microcentrifuge tubes (Eppendorf) to be stored at -80°C prior to sequencing. Samples were randomized and the RNA quality was verified using a High Sensitivity ScreenTape Assay on the Tape Station 2200 (Agilent Technologies) and measured with a NanoDrop 1000 (Thermo Fisher). Library construction was performed using the Universal Plus mRNA Library Kit (NuGen Technologies), and sequencing was performed on the NovaSeq 6000 instrument (Illumina) using paired-end sequencing (150 bp) by the University of Colorado Cancer Center Genomics and Microarray Core.

Illumina adapters and the first 12 base pairs of each read were trimmed using BBDuk<sup>43</sup> and reads <50bp post trimming were discarded. Reads were aligned and quantified using STAR (2.6.0a)<sup>44</sup> against the Ensemble mouse transcriptome (GRCm38.p6 genome (release 96)). Reads were normalized to counts per million (CPM) using the edgeR R package.<sup>45</sup> Differential expression was calculated using the limma R package and the voom() function.<sup>46</sup> In addition to two-group comparisons, an interaction model within limma was used to compare the differences between Dp16 and WT as a result of the infection ((Dp16 infected vs. Dp16 non-infected) vs (WT infected vs. WT non-infected)). Fast Gene set enrichment analysis (fgSEA) was performed using the fgSEA R package (v1.10.0) with 10,000 permutations<sup>47</sup> with Hallmark or GO Biological Process gene sets from the Molecular Signatures Database.<sup>48</sup> Heatmaps were generated with the ComplexHeatmap R package following z-score transformation of CPM data.<sup>49</sup>

### Luminex multiplex cytokine and chemokine assay

An array of cytokine and chemokine factors were analyzed in undiluted mTEC basal medium samples that were collected 48 hrs after infection. Immune Monitoring 48-Plex Mouse ProcartaPlex™ Panel (Thermo Fisher) was used for medium analysis and samples were run on a Luminex MAGPIX system through the University of Colorado Cancer Center Flow Cytometry Core at the Anschutz Medical Campus. Basal

medium aliquots were thawed, and samples were randomized on a 96 well plate for processing via manufacturer's protocol.

### **Ciliary beating frequency measurement**

Ciliary beating was observed using Leica TCS SPE DMI8 (Leica) confocal microscope equipped with ORCA-Flash4.0 V3 Digital CMOS camera (Hamamatsu) and a 20× dry objective. The microscope was outfitted with a custom environmental containment chamber (Oko Labs) to control humidity, temperature, and carbon dioxide (CO<sub>2</sub>) to mimic culture conditions and prevent variation in ciliary beating. The TWIs to be imaged were placed inside the environmental control chamber on the microscope stage. 512 x 512-pixel images of ciliary beating ( $\geq 3$  per TWI) were acquired at an average frequency of 100 fps (Hz) via LASX software suite (Leica) and the data were subsequently exported to be analyzed at Matrix Laboratory (MATLAB).

A custom-designed MATLAB code was developed to analyze the ciliary beating videos. The code analyzed each video frame-by-frame, pixel-by-pixel and detected active areas of movement within the video as well as the oscillating frequency of the movements observed. These data are then used to generate a heatmap for each video, which displays frequency distribution of ciliary beating with color codes each representing a distinct beating rate (in Hz) (Figure 3A).

The code contained a set of .m files, with the main file and the start of the code being within the function ProcessCiliaryBeatFrequency. At the top of the function the file name, path, and file type were specified along with the frame rate of the video, other parameters such as pixel resolution were automatically calculated from the video file. The function ProcessCiliaryBeatFrequency then generated a 3D array of data for the x, y, and frame dimensions of the video file and converted to gray scale. The standard deviation was then calculated for each pixel as a function of the frames. The standard deviation was then scaled to fit within the byte value for a gray scale image, as the standard deviation data was visualized as a grayscale figure as an intermediate output of the code.

Next the grayscale video 3D array was passed into a function called DiscretizeFrequencyPixelSections along with the frame rate and the grouped pixel size, in this case the grouped pixel size was one, meaning the function computed the frequency of each pixel, but had the capability to group pixels and calculate the grouped frequency. Within DiscretizeFrequencyPixelSections, the group pixels were iterated through, in this case only on a pixel-by-pixel basis, with a Fast Fourier Transform (FFT) using a Hanning window to calculate the frequency response of each pixel. The FFT returned intensity as a function of frequency; in the videos processed while there was a relatively tight distribution within the frequency response, we still observed some noise. In order to process the data, a bandpass filter of 2 Hz to 50 Hz was then applied and the mean of the frequency response was subtracted from the data to remove any noise. This not only helped us remove the noise (that is not from the CBF) but also to take out the static offset in intensity applied uniformly across the frequency response. With the remaining non-zero frequency data, we applied a center of mass calculation to the frequency response to generate a single weighted frequency data point; this was the same as taking the mean of the intensity multiplied by the frequency at each data point and dividing by the mean intensity of the entire data set. This resulted in a single weighted frequency data point per pixel.

After calculating the frequency response of each pixel, the 3D array of standard deviation of each pixel as a function of the frames was used as a mask for the calculated frequency response of all the pixels as a function of frames. This was done within the DetectBeatingCells function, where the standard deviation of data was converted into a binary image with a cut-off of 1 for the standard deviation of a pixel, where the pixels were represented by a byte. This binary image was then used as an active area mask, only the pixels that were above the threshold were considered active, otherwise the fluctuations of the signal were determined to be too weak and not related to ciliary beating.

The masked frequency pixel data was then converted to a heatmap and overlaid on a frame from the video to generate a heat map figure. Two sets of output data were also generated, the ratio of active area and the binned ciliary beat frequency distribution. The ratio of active area is calculated from the binary image displaying the active area within the FOV. The binned data was a sum of all the pixels within the video binned by frequency at a 1 Hz separation. The data is saved to an Excel file.

### Mucociliary transport measurement

Mucociliary transport (MCT) was quantified using 0.2  $\mu\text{m}$  FluoSpheres™ Carboxylate-modified Microspheres in yellow-green fluorescent (Thermo Fisher) diluted 1:1000 in mTEC Basic Medium. Each TWI was briefly received 50  $\mu\text{L}$  of the nano-bead mixture on the apical surface of cultured epithelia before removing the beads. The plate positioned onto the stage of a Leica TCS SPE confocal microscope inside of the environmental containment chamber as described above (that generated maximal humidity, 37°C and injects 5%  $\text{CO}_2$ ). The yellow-green fluorescence was excited using the 488nm laser and microsphere movement was recorded via 20 $\times$  objective and LASX software capturing videos averaging 20 seconds in length at high frequencies. Videos were then exported and analyzed using FIJI Trackmate<sup>50</sup> with an additional extension (TrackAnalysis<sup>51</sup>) to quantify total distance traveled for each track. Parameters for analysis were held constant throughout video processing and beads captured by cilia were filtered out using track displacement metrics. Based on cell size and ciliary length any track with a displacement of less than 30 $\mu\text{m}$  was eliminated to ensure quantification of cells that are being moved via MCT. Total distance traveled via the remaining tracks was recorded and processed to give MCT in  $\mu\text{m}/\text{seconds}$ . Finally, video overlays of bead tracking were recorded and stored (Video S1).

We used two sets of controls in our studies for CBF and MCT analysis. One was cell-free transwell inserts and the other was confluent, un-differentiated (non-ciliated), mTECs on TWIs. We captured videos of ciliary beating and particle movement to identify non-specific movements that need to be avoided when calculating CBF and MCT values. In addition, for MCT analysis, as shown in Video S1, we followed trajectory of nanobead movements and those with clear path were analyzed for plotting MCT rates. As such, stochastic, non-ciliary motility is excluded in our approach.

### QUANTIFICATION AND STATISTICAL ANALYSIS

To obtain  $n = 6$  transwell inserts, we sacrificed and combined tracheas from 3–5 mice during tissue dissociation so that adequate cells are present to differentiate *in vitro*, and when experiments were performed on independent sets of mice, they were clearly stated in figure legends. Statistical analysis on qPCR (on apical virus shedding), flow cytometry (on frequency of ciliated cells in mTECs), gene expression (RNA-seq transcript levels), multiplexed bead-based protein levels (cytokine/chemokine secretion) and MCT was performed by non-parametric *Mann-Whitney* and unpaired two-tailed Student's *t* tests using GraphPad PRISM. The data were considered statistically significant when  $p < 0.05$  (\* $p < 0.05$ , \*\* $p < 0.01$ , \*\*\* $p < 0.001$ , \*\*\*\* $p < 0.0001$ ). Differential gene expression was done using the LIMMA package (a moderated *t* test).

Statistical analysis on CBF was performed by processing the generated data containing binned pixel CBF response with another MATLAB script to allow for GraphPad PRISM compatibility. The data was ultimately displayed as pixels per field of view (FOV) as a function of CBF binned at 1 Hz, with the distribution of CBF centered at the average CBF for that data set. Quantile-Quantile (QQ) Plots were generated to show the deviation of each distribution from a normally distributed data set (Figure S3).

The MATLAB code was contained in a single function within the file ProcessBinDataIntoRawRoundedData.m and it was used to (1) generate data in a format acceptable by GraphPad PRISM and (2) format Microsoft EXCEL files for simplified insertion into Prism. The function went through all binned data sets that were from the same conditions (e.g., WT) and generated the rounded-to-nearest 1 Hz CBF without ordering – i.e., the generated data set may contain repeated CBF data points for the number of times it occurred. However, due to data point limitations in GraphPad PRISM, a single data point was generated per 10 identical data points – e.g., if 10 Hz occurred on 30 pixels then the processed data would be 3 identical 10 Hz data points. The data was then organized by individual FOVs as well as all combined FOV for a condition and exported as Microsoft EXCEL files.

The 'DataComparison' named files were generated to study variance within each FOV, specifically combined CBF data within a condition and the same data but centered around the median CBF for that condition. Additionally, Microsoft EXCEL files were generated for each condition, and the file names were formatted as '[condition]\_' with 'MedianOffset', 'Processed', or 'Statistics' appended to the file name. These files contained the CBF data for each FOV centered around the median CBF in 'MedianOffset', the same data without the median offset in 'Processed', and the standard deviation and variance of each field of view in 'Statistics'.

Within GraphPad PRISM, the output of the ProcessCiliaryBeatFrequency, specifically the binned data at 1 Hz, is plotted for each of the conditions, where error between each FOV within a condition was used as error bars. The data from the file 'DataComparison\_TotalMedianOffset' was also plotted as a column scatter plot for each condition. The data had a histogram analysis performed, as well as a normality test and *Kruskal-Wallis* test, due to the normality test failing. QQ plots were generated from the 10-pixel grouped processed data from ProcessBinDataIntoRawRoundedData for each condition showing each of the FOV overlaid within a single condition.